Optical properties of perovskite layers in patterned devices

Universität Konstanz

Bachelor thesis

Submitted at the University of Konstanz by

Georg-Michael Krause

Prof. Dr. Bruno Ehrler (AMOLF Institute Amsterdam)

Prof. Dr. Lukas Schmidt-Mende (University of Konstanz)

Supervision: Dr. Loreta Muscarella

March 9, 2022

Abstract

In the rapidly progressing field of lead-halide perovskite materials, optical confinement of photons inside the active layer still highly limits efficiency of device application. This thesis introduces periodic SiO_2 nano-structures imprinted onto the hole injection layer in the LED, thus structuring the active perovskite material ($MAPbBr_3$). As the main result of this work, the proof of concept is given that the loss-mechanism of light-trapping inside the active layer can instead be used to control directionality of photo-luminescent emission of perovksite LEDs. Controlled emissive directionality is found to be a direct effect of wave-guide mode scattering due to the periodic SiO_2 grid inside the $MAPbBr_3$ layer. Based on (free) photon dispersion and the extended Brillouin-zone scheme of the hexagonal perturbation structure, strikingly accurate predictions on directionality of scattered wave-guide modes can be made. These predictions are confirmed by experiment using back-focal plane imaging in a Fourier microscope setup, where the in-plane k-vector intensity distributions are measured. In addition, it is shown that imprinted nano-structures inside the $MAPbBr_3$ layer of the LED stack improve light out-coupling efficiencies by a factor of $f = 2$ in photo-luminescence experiments. To add to the versatility of the SCIL-imprinting technique used in this thesis, it is proven that the introduction of a nano-structure does not change prominent opto-electronic properties of the $MAPbBr_3$ layer. The SRH-lifetime of patterned $MAPbBr_3$ shows $\tau = 18.4$ns, whereas flat $MAPbBr_3$ features $\tau = 24.6$ns in TCSPC experiments. Band-gap energies E_G are measured to be $E_G = 2.32$eV for both types of perovskite layer in UV-vis absorption measurements. XRD measurements cannot resolve differences in crystallization.

Trotz rasanter Fortschritte auf dem Forschungsgebiet der Organo-Halogenid-Perowskite ist die Effizienz der auf diesen Materialien basierenden LEDs stark durch hohen Lichteinschluss innerhalb der photoaktiven Schicht beschränkt. Durch Nanolithografie von Siliziumdioxid (SiO_2) direkt auf der Loch-Transportschicht innerhalb der LED zeigt diese Arbeit eine innovative Möglichkeitv auf, die photoaktive Schicht zu strukturieren. Als zentrales Ergebnis dieser Arbeit wird dargelegt, dass durch diese Strukturierung der Verlustmechanismus des Lichteinschlusses genutzt werden kann, um die Abstrahlungsrichtung der LED zu kontrollieren. Basierend auf der (freien) Dispersionsrelation von Photonen und dem erweiterten Brillouinzonenschema der aufgeprägten, hexagonalen Struktur können Abstrahlungsrichtungen sehr genau vorhergesagt und mit der zugrundeliegenden Bandstruktur vollständig erklärt werden. Die Verifikation der Vorhersage erfolgt im Experiment, indem die planare Wellenvektorverteilung k der Abstrahlung im Fourier-Mikroskop gemessen wird. Des Weiteren wird in Photo-Lumineszenz Experimenten gezeigt, dass durch die Strukturierung der Perowskitschicht eine Effizienzsteigerung vom Faktor 2 erzielt werden kann. Die Anwendbarkeit der Nanolithographie mit SiO_2 wird demonstriert, da keine signifikanten Änderungen der optischen und elektrischen Eigenschaften des Materials experimentell gefunden werden können. Die SRH Lebensdauern, welche in TCSPC Experimenten bestimmt werden, zeigen $\tau = 18.4$ns für die strukturierte und $\tau = 24.6$eV für die unstrukturierte Perowskitschicht. The Bandlücke von $E_G = 2.32$eV bleibt unverändert durch die Strukturierung, wie in UV-vis Absorptionsmessungen gezeigt wird. Auch die Kristallisierung der $MAPbBr_3$-Schicht, welche in XRD Experimenten gemessen wird, zeigt keine messbare Abweichung durch Strukturierung.

Contents

1 Introduction

The human-made climate change demands for immediate action. In that sense, research is in charge to develop cheap, yet efficient and reliable market-ready technologies. These could advance existing strategies to cut greenhouse gas emissions and therefore limit global warming. Further, advanced sustainable technology could even open up new pathways in this fight against the clock.
A recent, promising topic in the field of sustainable technology are lead-halide perovskite materials. Due to their prominent opto-electronic properties such as their high purity in color, tunable band gap and carrier mobility [SAM+15] as well as their low cost and straight-forward fabrication [LXB+21], research on lead-halide perovskite materials has advanced substantially in recent years [WLSS17]. Pushing energy conversion efficiencies to values of over 20% [CZT+20] and therefore surpassing state-of-the-art silicon-based thin-film technologies [NRE], lead-halide perovskites provide for promising application in solid-state electronic devices such as solar-cells and LEDs.
Yet in this domain of research, there are also huge challenges ahead such as chemical instability of perovskites under ambient and working conditions and their toxicity for the environment [LXB+21]. With regard to perovskite LEDs in particular, optical confinement of emitted photons due to the high refractive indices of perovskite materials limits external quantum efficiencies [SCL+19]. However, metal halide perovskite films have shown exceptionally high quantum photo-luminescence efficiencies [KCL16]. As a consequence, overcoming optical trapping of emitted photons in perovskite LEDs is yet a field of research in which efficiencies could be enhanced significantly [MLT18].

This leads to the main goals of this thesis. In order to further enhance the field of application of perovskite LEDs, this thesis introduces SCIL (Soft Conformal Lithography Imprinting) applied inside the active perovskite layer. As the main result of this thesis, this work gives proof to the concept of guided photo-luminescent emission out of patterned perovskite layers. We show that guided photo-luminescent emission is a direct cause of SCIL imprinting as the imprint introduces a periodic perturbation inside the perovskite layer. Scattered wave-guide modes, being a consequence of periodic perturbation inside the perovskite layer, are then quantified in photo-luminescence measurement setups with angular resolution (plane k-space). As a consequence and logical step of the findings presented in this thesis, guided electro-luminescent emission due to wave-guide mode scattering could be introduced into several LED-applications. Specifically structured perovskite layers could eventually be used for enhanced surface-normal emission

as an example of the future.
Additional to the possibilities of guided emission through structuring, this thesis shows the potential of SCIL imprinting as a strategy to improve light-outcoupling out of LED stacks in order to push external quantum efficiencies of perovskite LEDs.

1.1 Enhancing light out-coupling: Patterns in perovskite layers

The figure-of-merit for LED efficiency is the so-called external quantum efficiency (EQE). EQE is defined as the number of generated photons $p_{\mathrm{g,ex}}$ escaping the device divided by the number of electrons e_{in} injected into the device [MLT18]: $EQE = \frac{p_{\mathrm{g,ex}}}{e_{\mathrm{in}}}$. EQE can be qualitatively explained using the following relation [MLT18]:

$$EQE = IQE \cdot OCE \tag{1.1}$$

As the upper equation suggests, the efficiency of an LED is affected by two key parameters, IQE and OCE. IQE stands for internal quantum efficiency. In comparison to the external quantum efficiency, IQE is defined as the number of generated photons p_{g} inside the perovskite layer divided by the number of electrons e_{in} injected into the device, $IQE = \frac{p_{\mathrm{g}}}{e_{\mathrm{in}}}$ [ARH+19]. It is normally higher than EQE since photons can be reabsorbed or get optically confined on their way out of the device. IQE is a measure for the energy-conversion efficiency of the perovskite material [ZZF+20][MLT18]. The second parameter is OCE (out-coupling efficiency). It gives the probability of photons to exit the device, thus it is the ratio of photons escaping the device $p_{\mathrm{g,ex}}$ to photons generated inside the perovskite layer p_{g} [ZZF+20].
Regarding IQE and OCE for high efficiency devices, the focus in this work is set on the limiting factor of light out-coupling (OCE). Three material properties of the LED stack change OCE significantly [ZZF+20]. The first property are the differences in refractive index n between layers of the LED stack. Most importantly, poor refractive index alignment of materials leads to optical confinement of a high fraction of photons that are generated in the active layer. Thus, only a low number of photons are actually out-coupled and exit the device. Additionally, the layer thicknesses inside the LED stack and the emitter-dipole alignment within the perovskite layer play a major role in the out-coupling efficiency (OCE) [MLT18]. Thus, the motivation of this project lays in finding new ways to improve OCE.
Optical confinement of photons generated in the active layer is mostly induced by total internal reflection (TIR) due to insufficient alignment of refractive indices n between layers of the LED stack. Prominent terminology defines the "wave-guide mode" which

refers to photons confined in the active layer and transparent ITO electrode. Further, the "substrate mode" refers to optical confinement inside the glass substrate of an LED and the "air mode" describes the photons being coupled out of the system, therefore surpassing the glass-air interface. Further losses and modes are caused by absorption or "surface plasmon polarion modes" (SPP) at the metal interface [ZLR+19][MLT18]. Additional to that, effects such as photon recycling, meaning re-absorption by photons resulting from radiative recombination to trigger another excitation, have to be taken into account[CZT+20]. For explanation and visualization reasons of these wave modes only, we will assume that layer thicknesses of the LED stack are in the mm-range. Doing so, geometrical optics (thicknesses of layers>> λ) can be applied and wave-guide modes be drawn as light rays inside the stack. However in real application, LED layer thicknesses feature the same scale (nm) as the wavelength (nm) itself. Thus, one has to account for the near-field distribution inside the LED stack, e.g. done in [MLT18]. In the following, the wave modes discussed above are shown assuming geometrical optics for explanation reasons:

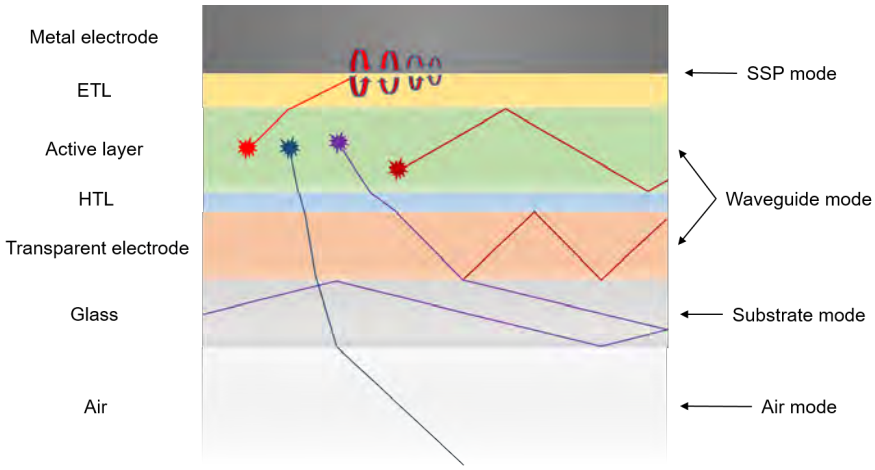

Figure 1.1: Simplifying visualization of wave modes in a LED stack, assuming geometrical optics (layer thicknesses in mm range) for explanation reasons. The modes presented still do not account for effects such as re-absorption or photon recycling [MLT18].

As can be seen in figure 1.1, emitter-dipole orientation inside the active layer plays a crucial role for light out-coupling (photons reaching air mode) as has been also shown theoretically by [MLT18]. Since perovskite active layers feature refractive indices of $n \approx 2.5$, low in-plane k-values of the propagating wave are decisive for reflection or

transmission at interfaces. Owing to a high refractive index n in perovskites, proper alignment of refractive indices n between layers inside the stack can significantly reduce SPP modes and increase out-coupling towards the glass side, e.g. by introducing an ETL-layer featuring a significantly lower refractive index compared to the perovskite layer. According to [MLT18], lowering n_{ETL} holds for all wavelengths λ. Increasing the refractive index of the HTL (n_{HTL}), light-outcoupling can be risen for blue and green emission. This applies to the case discussed in this thesis since a green emitting perovskite compound ($MAPbBr_3$, $\lambda \approx 535$nm) is used. It would be intuitive to assume that a higher n_{HTL} would grant for better outcoupling over the whole wavelength spectrum. This behavior of the stack is not completely understood, yet it is likely due to the dispersion of perovskite materials [MLT18].
Introducting a periodic structure inside the perovskite layers in this thesis, we aim for advanced light out-coupling of wave-guide modes out of the active layer. Altered propagation paths of the light due to patterning inside the active layer lead to different incident angles of the light on the HIL-glass interface and therefore also influence the fraction of substrate modes and air modes [MLT18] (HIL = hole injection layer).
Several out-coupling techniques which focus on structuring of devices have been recently introduced. One approach very closely linked to the SCIL patterning approach presented in this thesis is a work by [MLT18] and [SCL+19]: A moth-eye nano-structuring of the cesium lead bromide active perovskite layer. The structuring was introduced by a patterned ZnO underlay. In their case, the ZnO layer served not only as the structure itself, but also as the hole injection layer of the perovskite LED [SCL+19][MLT18]. Their moth-eye structuring is reported to induce significant improvements in simulation and experiment regarding the out-coupling of wave-guide modes inside the active layer, therefore resulting in higher EQE. Intriguingly, their work shows that wave-guide modes can be reduced over the whole visible spectrum of wavelengths λ in simulation using one and the same structure.
To draw on the findings of [MLT18] shown above, this thesis equally introduces a hexagonal patterning structure with slightly altered periodicity and pillar height. Different to [MLT18], we pattern the perovskite layer directly by using an inter-layer between an unstructured hole injection layer and the active perovskite layer. The structure consists of patterned silicon dioxide (SiO_2). This provides for higher versatility of structuring inside LED stacks since the patterned SiO_2-layer can be applied everywhere in the stack, based on the needs of its application. Secondly, our technique can be applied independent of the hole injection layer being organic or inorganic whereas the patterning approach of [MLT18] is limited to inorganic materials only. Additional to that, we not only show the

out-coupling properties of the SiO_2-pattern, but more importantly the pattern's scattering properties of wave-guide modes. Thus, optical confinement inside the structure which is normally seen as a loss mechanism is turned into a strategy to specifically guide emission out of the device. The angles of emission can be directly steered by the design of the pattern that is imprinted. The results of scattered wave-guide modes into far-field radiation could open up new possibilities in LED design to guide emission.

1.2 Main objectives

As a proof of concept, the main objective of this thesis is to show that guided photo-luminescent emission out of perovskite LEDs can be achieved by periodic structuring of active perovskite layers. Applying back focal plane imaging, the distribution of photo-luminescent intensity in plane k-space is measured to proof the possibility of guided, photo-luminescent emission experimentally. As an essential step to achieve a sharp scattering picture of wave-guide modes, we show that employing SCIL imprinting using silica-based sol-gel resists is suitable for highly uniform and well-defined pattern fabrication underlying perovskite layers. In this regard, we proof experimentally that electric contact between the perovskite layer and the underlying hole injection layer can be made through the pattern itself as this is crucial for the feasibility of SCIL in perovskites.

1.3 Complementary objectives

To make sure that the results we observe can be attributed to the pattern itself, X-ray diffraction (XRD) and UV-vis absorption spectroscopy are used to identify possible differences in substrate-plane crystal growth as well as differences in absorption that might occur due to the pattern. As a further result, charge-carrier lifetime differences between structured and unstructured perovskite layers are investigated using time-correlated single photon counting measurements (TCSPC). Possible lifetime differences could thus give valuable insights into the passivation properties of the sol-gel layer and thus, if this SCIL sol-gel imprinting method features general applicability. As a last step, the photo-luminescent emissive intensities of different light-cones with regard to the absorption differences of patterned and un-patterned perovskite films are compared in order to quantify light out-coupling properties of the structure used in the experiments.

2 Theory

2.1 Perovskite crystal structure, optical properties of $MAPbBr_3$

Lead halide perovskites are suitable for optoelectronic application mainly due to their very narrow emission spectra (FWHM $\approx$ 20nm) and high energy conversion efficiencies [KCL16].
The aristotype perovskite structure is a crystal which forms by the ABX_3 stochiometry, meaning corner sharing octahedra (BX_6). In its overall cubic structure (conventional cell is cubic), the unit cell, consisting of 5 atoms, can thus be described as the monovalent A-cation residuing at a corner, the divalent B-cation being positioned in the cubic center and 6 anions in the center of each plane of the cube [AM20]. This is shown in the following:

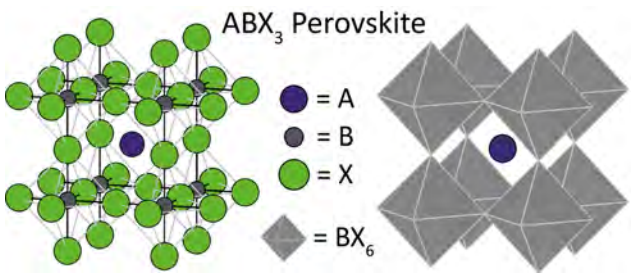

Figure 2.1: Aristotype perovskite cubic structure in ABX_3 stochiometry: Monovalent cation A is placed in a corner of the cube, divalent cation B in the middle of the cube. 6 anions are positioned in the center of the planes of the cubic structure, building an octahedron.[AM20]

Metal halide perovskites, being a subtype of perovskite materials themselves, can be processed in several variants such as vacant and/or ordered perovskites. The size of the A-cation in the ABX_3 bulk is a limiting factor for gemotrical, stable crystallization. Another factor which affects stability of perovskites is the octahedral factor which concerns stability of the octahedron (BX_6) itself. As an example, first row transition metals such as titanium(Ti) being ordered by large anions such as Br^- rather crystallize in tedrahedral manner[AM20].
Hybrid organic-inorganic perovskites combine advantages of both material types such as high charge-carrier mobility of inorganic matter and ease of processing of organic matter which are both crucial for optoelectronic application [KCL16]. In this work, methyl-ammonium lead tribomide ($MAPbBr_3$) is used. As discussed above, the larger Pb^{2+} compared to the MA^+ cation leads to stable ABX_3 crystallization. This kind of

ammonium - lead - trihalides form bulk 3D perovskites. When employing a mixture of differently sized cations for the A site of the ABX_3 general structure, one can further achieve layered metal halides consisting of a small cation (e.g. MA^+) forming perovskites which are then spaced by the larger, organic cations such as PEA. These structures are usually referred to as 2-D perovskites and exhibit better stability in moist conditions as well as enhanced work-function tuning compared to 3D perovskites [AM20].
Looking at characteristic opto-electronic properties of $MAPbBr_3$, the band structure of this lead-halide perovskite determines the emissive behavior of the material.
Regarding absorption in experiment using single crystal ellipsometry, $MAPbBr_3$ single crystals show three main absorption peaks which can be then attributed to inter-band recombination [LAA+16]. As shown in figure 2.2, the band-structure of bulk lead-halide

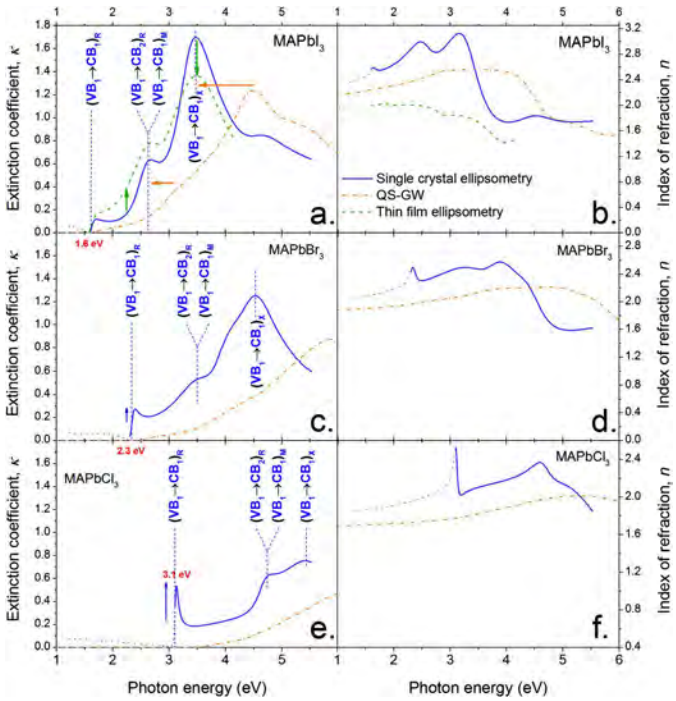

Figure 2.2: Extinction coefficient κ and refractive index n of MAPbBr−3 and further hybrid perovskites plotted on y-axis for different photon energies[eV] on x-axis resulting from ellipsometry (blue solid line) and simulation (brown dashed line). Absorption peaks can be matched to simulation of band-structure as indicated using VB (valence band) and CB (conduction band). Graph by [LAA+16]

perovskite materials is strongly dependent on the halide anion.
To tune the absorption edge of the material to the need of its application, the halide ratio can be mixed in order to achieve the optical properties aimed for (X_3-site). Pho-

toluminescent emission in perovskites mainly results from radiative bi-molecular recombination of unbound electrons and holes, meaning that both one electron and one hole are involved in the process. This is due to very low exciton binding energies (<40meV) compared to e.g. organic semiconductors (>100meV). Thus, laser excitation leads to direct photo excitation rather than exciton separation [WCD+22]. The optical transition in $MAPbBr_3$ which is of particular interest for emission in the visual spectrum is right at the absorption edge shown in fig. 2.2, leading to an emission at $\lambda \approx 530 - 540$nm in photo-luminescence experiments.[WLSS17]. As can be seen from band-structure simulations by [LAA+16], $MAPbBr_3$ and lead-halide perovskites work as direct band-gap semi-conducting materials. They therefore provide for excellent tunability in emission [WX19].
The FWHM of photo-luminescent emission at 540nm of $MAPbBr_3$ is reported to be around $15 - 20$nm. Considering a FWHM > 40nm in state-of-the-art organic LEDs, $MAPbBr_3$ promises for high color purity in further application[WLSS17][KCL16]. The color purity results from higher energetic order of excited states in perovskites compared to organic emitters, mainly due their higher crystallinity and less localized charges which lead to reduced photon-electron coupling that broadens the spectrum[WCD+22]. More importantly, the width of emissive wavelengths is not significantly interfered by trap-assisted recombination or other defects in $MAPbBr_3$ films. This is mainly due to the fact that recombination related to insufficient crystallization is mostly non-radiative [KCL16]. The delocalization of charges in perovskites, due to high structure, high charge carrier mobilities ($0.1 - 10\text{cm}^2\text{V}^{-1}\text{s}^{-1}$) and low exciton binding energies, finally leads to highly efficient perovskite LED and perovskite solar cell applications with active layer thicknesses of >500nm [WCD+22][WX19].

2.2 Semi-conductors and n-i-p stuctures: band-alignment, electron and hole concentrations

Perovskite LED device-architecture aims to integrate device stability and device efficiency into the LED system. The most common architecture for perovskite LEDs can already be found in OLEDs and solar cells, which are based on luminescent p-i-n diodes or p-n-junctions respectively. The fundamental LED implementation of the p-i-n diode is displayed in the following:

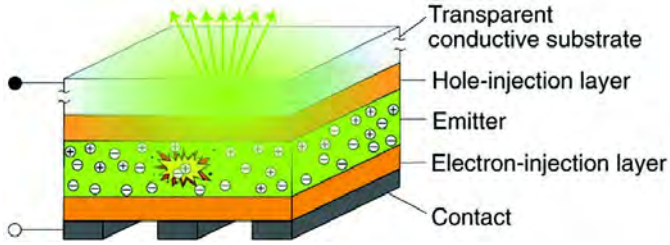

Figure 2.3: Device architecture p-i-n perovskite LED: Light-emitting layer (EML, intrinsic) enclosed by (doped) charge transport layers. The hole-injection layer (HIL) placed towards the anode, the electron-injection layer (EIL) placed towards the cathode. The transparent anode provides for light-extraction out of the system. Graph by [JAAS21]

LEDs emit light due to radiative recombination of electrons and holes. Due to the high diffusion length of carriers in perovskites, charges move in rather band-like manner [WCD+22]. In order for electrons and holes to recombine inside the perovskite layer as depicted in figures 2.4 and 2.3, the band alignment of the HIL and EIL relative to the perovskite layer plays the crucial role. Electrons are injected through the cathode into the ETL and propagate into the perovskite layer. Vice versa, holes are induced into the HTL and move further into the perovskite. Efficient carrier injection is achieved if electrons energetically move down transitioning from ETL to the perovskite layer and holes energetically move up. An example of the band alignment of an optimal hetero-junction p-i-n device for LED application is shown in figure 2.4. The ideal double hetero-junction

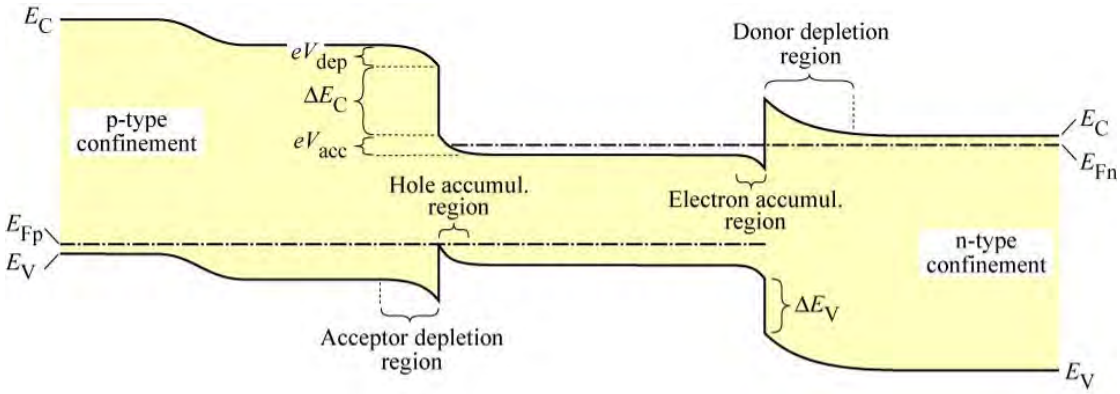

Figure 2.4: Hetero-juction under forward bias: n-type semi-conducting material on the right, p-type semi-conducting material on the left. The n-type material, serving as an elecron injector as well as a hole blocking layer through band-alignment and the p-type material vice-versa. Graph by [Sch06]

of semi-conducting materials forces electrons and holes into the i-type active material. The Fermi-energies E_{Fn} and E_{Fp} do not align since the device is under forward bias, thus injecting electrons from the n-type semi-conductor side into the i-type region and overcoming the donor depletion region. On the same hand, holes are injected from the left, under forward bias overcoming the acceptor depletion region. The band-bending on the interfaces is depicted in a qualitative manner, as their bending depends on the Fermi-levels and the permittivity ϵ of each individual material [ARH+19].

2.3 Photo-luminescence and TPL

2.3.1 Photo-luminescence: definition and explanation

Photo-luminescence (PL) measurements are essential for understanding charge-carrier kinetics and recombination processes inside semi-conducting materials. In PL measurements, photo-excitation (e.g. laser-excitation) is used to excite charges or separate excitonic states inside a semi-conducting material. The radiative emission resulting from radiative recombination of these excited charge-carriers is then measured. Among several factors, the most important parameter which has to be controlled and measured during PL experiments is excitation density. This is due to the fact that excitation density affects recombination processes and kinetics severely [KMSU20].
Recombination processes and carrier densities can be investigated using transient photo-luminescence measurements (TPL). Photo-luminescence decays in TPL are measured using time-correlated single photon counting (TCSPC). In TPL measurements, one only measures radiative emission decays. Therefore, mathematical models have to be introduced to also make quantitative statements on dominating non-radiative recombination processes related to the radiative decay which is observed. This enables to qualitatively compare dominating recombination processes at different times of the PL decay when measuring the samples in TCSPC. Further, lifetimes can be quantitatively derived by fitting this decay model to the data received in TCSPC. Finally, conclusions can be drawn on possible differences in carrier lifetime and recombination processes comparing SCIL patterned perovskite layers and flat perovskite layers to each other. Thus, the effect of the imprinted SiO_2 on the quality of the perovskite-SiO_2 interface as well as the quality of the perovskite layer grown on top of imprinted SiO_2 can be compared to non-imprinted devices. This is valuable information since it provides insights on passivation properties of SCIL-imprinted SiO_2 layers which is a vital factor for the applicability of this SCIL-patterning method in perovskite devices.

2.3.2 TCSPC measurements and modeling recombination mechanisms: radiative, SRH, Auger

The general idea in modeling the transient PL-decay lays in the continuity equation. It aims to sum up excitation rates, recombination rates, re-excitation rates, drift and diffusion of carriers when a semiconductor material is being photo-excited [KMSU20]:

$$\frac{\mathrm{d}n,p}{\mathrm{d}t} = G_{ex}(t,x) + G_{int}(t,x,n,p) - R(t,x,n,p) + D_{n,p} \cdot \frac{\mathrm{d}^2 n,p(t,x)}{\mathrm{d}x^2} + F \cdot \mu_{n,p} \cdot \frac{\mathrm{d}n,p(t,x)}{\mathrm{d}x} \tag{2.1}$$

In equation 2.1, G_{ext} refers to the rate of externally generated electrons or holes, G_{int} to the rate of internal re-generation of electrons or holes (as an example: photon recycling). Drift of carriers, proportional to the electric field F and the gradient of carrier density $\frac{\mathrm{d}n,p(t,x)}{\mathrm{d}x}$ and diffusion of carriers, proportional to the change of carrier-density gradient in space ($\frac{\mathrm{d}^2 n,p(t,x)}{\mathrm{d}x^2}$), are scaled using drift and diffusion constants $\mu_{n,p}$ and $D_{n,p}$. Lastly, carrier-recombination is included by summand D. This continuity equation still does not consider (de)-trapping, yet since lifetimes in perovskites are in the region of >1ns, (de)-trapping kinetics are negligible [KMSU20].
On samples which only feature perovskite layers on glass substrates, drift terms are insignificant since there is no build-in electric field across the active perovskite layer, meaning $F = 0$. Since perovskites further are intrinsic, photo-excited hole and electron concentration can be assumed to be somewhat equal. Expecting high excitation densities during PL measurements, one can approximate that there is no significant gradient in hole or electron density on the probe spot. Thus, the following approximation holds: $n(x,t) = n(t) \approx p(x,t) = p(t)$ [KKL+21]. Therefore, equation 2.1 can be simplified significantly to the following, now neglecting dependence in position x [KMSU20]:

$$\frac{\mathrm{d}n,p}{\mathrm{d}t} = G_{ex}(n,t) + G_{int}(n,t) - R(n,t) \tag{2.2}$$

Three main recombination mechanisms have to be taken into account regarding recombination rate R: Bi-molecular radiative recombination, (deep) trap-assisted Shockley-Read-Hall (SRH) recombination and Auger-recombination. As SRH recombination only involves one carrier, it is plausible to put $R_{SRH} \propto n,p$. For bi-molecular radiative recombination (one hole and one electron involved), one can thus conclude: $R_{rad} \propto n \cdot p$. For Auger recombination, where 3 charge carriers are involved, the dependence on charge-carrier density can be modeled as cubic. The general expression for these three recom-

bination mechanisms can thus be summarized as follows: [KKL+21]:

$$R = k_{rad}(1 - q_{int}) \cdot (np - n_i^2) + \frac{(np - n_i^2)}{n\tau_p + p\tau_n} + (C_n n + C_p p) \cdot (np - n_i^2) \tag{2.3}$$

In equation 2.3, the first term regards radiative recombination. r_{rad} and q_{int} describe the radiative recombination and internal re-absorption coefficients respectively. Radiative recombination gets diminished by $(1 - q_{int})$ due to internal re-generation of carriers which are therefore subtracted from the bi-molecular recombination rate. The second term in equation 2.3, effectively linear in carrier density, describes SRH trap-assisted recombination where τ_p and τ_n stand for SRH hole and electron lifetimes, respectively. Auger coefficients C_n and C_p paired with either the product nnp or pnp where two electrons and one hole or vice versa two holes and one electron are involved in the recombination process, describe Auger-recombination. The third term is therefore cubic in carrier density.
In the high-level injection (HLI) regime of intrinsic semi-conductors such as perovskites, one can neglect dependence on the intrinsic carrier densities n_i and p_i, since $n >> n_i$ and $p >> p_i$ under illumination. Due to $n \approx p$ in perovskites as explained above, equation 2.3 simplifies to the following, analytically solvable expression [KKL+21]:

$$R = -\frac{\mathrm{d}n}{\mathrm{d}t} = k_{rad}(1 - q_{int}) \cdot n(t)^2 + \frac{n(t)}{\tau_p + \tau_n} + (C_n + C_p) \cdot n(t)^3 \tag{2.4}$$

Fitting equation 2.4 to the photo-luminescence decay measured in TCSPC, one can calculate $\alpha = k_{rad}(1 - q_{int})$ as the radiative coefficient, the effective SRH lifetime $\tau_{eff} = \tau_p + \tau_n$ and the possible Auger coefficient $C = C_n + C_p$ which should only have a major effect in very high illumination environments [KMSU20][KKL+21].
Qualitative interpretation of equation 2.4 can already be drawn without fitting the data: Since the three different recombination mechanisms are dependent on carrier density $n(t)$ by the powers of 1,2 and 3, Auger recombination (power 3) and radiative recombination (power 2) are expected to dominate recombination at early stages of the PL-decay when the initial carrier concentration is high. At later stages in time, linearly dependent SRH-recombination should dominate as carrier density n vanishes. Since the PL-decay Y_{PL} measured in TCSPC results from radiative recombination only, one can thus conclude $Y_{PL} \propto n \cdot p \approx n^2$. In later stages of the decay as SRH recombination dominates, we can thus state: $Y_{PL} \propto \exp\left(-\frac{t}{\tau_{eff}}\right)^2$. Thus plotting Y_{PL} logarithmically over delay time t, decays should trend towards linear slops at larger decay times. On the same hand, Y_{PL} should be non-linear in logarithmic plots at earlier stages t. This behavior is illustrated

by the following simulations of [KMSU20] and [KKL+21] in figures 2.5 and 2.6:

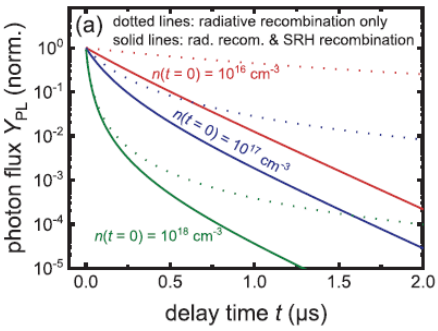

Figure 2.5: Impact of initial carrier density $n(0)$ on normalized Pl-decay Y_{pl} for given SRH lifetime τ_{eff} = const and given $\alpha = k_{rad} \cdot (1 - q_{int})$ = const; Graph by [KMSU20]

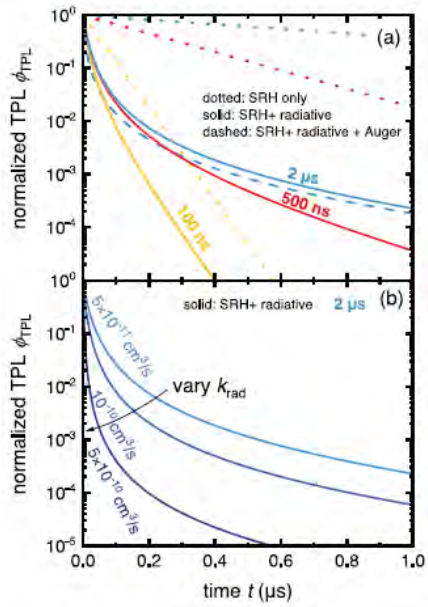

Figure 2.6: (a): Impact of SRH recombination only with SRH lifetime $\tau_{eff} = 100\text{ns}, 500\text{ns}, 2\mu\text{s}$. (b): $\tau_{eff} = 2\mu\text{s}$ and variation of k_{rad}; Graph by [KKL+21]

2.4 Optics

2.4.1 Pattern design

To prove the concept of measuring photo-luminescence scattering patterns out of SCIL-structured perovskite LED stacks, the following hexagonal pattern is used:

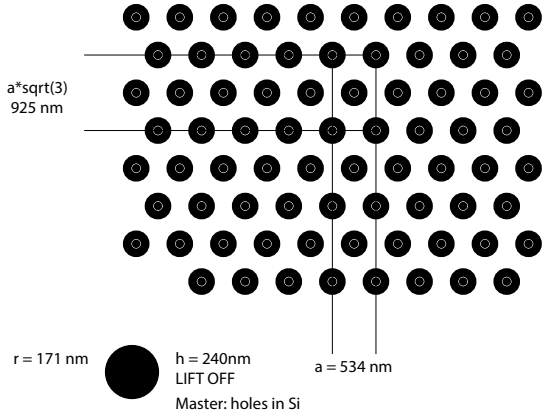

Figure 2.7: Hexagonal SCIL-pattern used for SCIL-imprinting: Imprinting the silica-based sol-gel resist with this pattern, a positive structure is created as shown in figure 3.6

The periodicity and pillar shape of the hexagonal pattern might not be decisive for the amount of out-coupled wave-guide modes. Recent out-coupling simulations of [MLT18] have shown that outcoupling of wave-guide modes inside the active layer works equally well for wavelengths of $\lambda = 400 - 800$nm using the exact same hexagonal pattern.
However, the wavelength λ as well as the pitch a of the pattern are both decisive for wave-guide scattering as they will define the Brillouin zone edges which are visible in the scattering image.
Consequently, we choose a hexagonal pattern for its proven out-coupling efficiencies. Yet, both the periodicity and the pillar dimensions were not specifically designed for favorable scattering characteristics but rather serve as a random pattern to prove the concept.

2.4.2 Diffraction limit

The resolution of nano-structures in a microscope is limited by diffraction. The diffraction limit gives a formula which describes the minimal distance, meaning the minimal dimension of a structure, to be resolved when imaged by the microscope. The minimal distance d of luminous structures which can be resolved according to the Rayleigh criterion is [ZZ18]

$$d = \frac{1.22\lambda}{2 \cdot NA} \tag{2.5}$$

with wavelength λ and numerical aperture $NA = n \cdot \sin[\Theta]$. Θ describes the half aperture angle, n the refractive index in which the objective is located [ZZ18]. Equation 2.5 is motivated by the Rayleigh criterion. It states that two (similar) objects can be resolved in space by a spectrometer if it diffracts the main maximum of the first object onto the first minimum of the other object [ZZ18].
The numerical aperture NA of an objective directly translates to the maximum in-plane k-vector of incident light that can be portrayed. Thinking of an optical setup with the z-axis being the optical axis, there is a maximum $\lambda_{\text{x,max}}$ which can be absorbed by the objective ($\lambda_{\text{x,max}} \cdot \sin[\Theta] = \lambda$) [Hec18]. Thus

$$\begin{aligned} k_{\text{x,max}} &= \frac{2\pi}{\lambda_{\text{x,max}}} \\ &= \frac{2\pi}{\lambda}\frac{\text{NA}}{n} \\ &= k \cdot \frac{\text{NA}}{n} \\ &= k \cdot \text{NA} \end{aligned}$$

if $n = 1$ for air.
As a last step, we can directly derive the diffraction limit of the luminescent SiO_2 pillars of the SCIL-pattern used in this thesis. With a wavelength $\lambda = 534$nm for photoluminescence of $MAPbBr_3$ and a numerical aperture used in back-focal plane imaging of $NA = 0.85$, the minimum resolvable distance d equals 383nm. Thus, with a distance between pillars (pitch) of 534nm in the SCIL pattern shown in figure 2.7, the wave-nature of light has to be taken into account, yet the pattern structure can be resolved.

2.4.3 Elastic scattering in crystalline structures: Laue condition

When light interacts with matter, it is either absorbed or scattered. Scattering of light at a wavelength λ is governed by the shape of the reciprocal lattice of a crystal and, if non scattered elastically, further affected by phonon excitation and absorption. Restricting this section to elastic light scattering, the law of momentum conservation $\vec{p} = \hbar\vec{k} = \hbar\vec{k'} = \vec{p'}$ has to be taken into account [GM12].
Assuming plane waves $\vec{E}(\vec{r}) = \vec{e_0} \exp[i\vec{k}\vec{r}]$ hitting a crystal lattice, the condition $|\vec{k}| = |\vec{k'}|$ must hold. This condition is, in elastic scattering processes, the criterion for possible $\vec{k}$ to $\vec{k'}$ transitions [GM12].

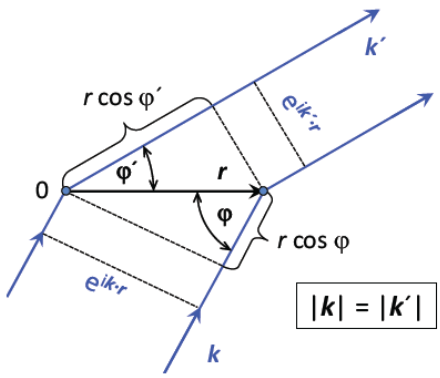

Figure 2.8: Constructive interference of plane waves between two points in the crystal lattice, elastic scattering assumed. Graph by [GM12]

From figure 2.8, $r\cos(\varphi) = \widehat{k}\vec{r}$ and $r\cos(\varphi') = \widehat{k'}\vec{r}$ can be deducted. As the path difference for constructive interference has to be an multiple of λ and $|\vec{k}| = |\vec{k'}| = \frac{2\pi}{\lambda}$, we can conclude that

$$(\vec{k'} - \vec{k})\vec{r} = 2\pi \cdot n \tag{2.6}$$

$$\exp\left[i(\vec{k'} - \vec{k})\vec{r}\right] = 1 \tag{2.7}$$

The comparison of equation 2.7 to the definition of the reciprocal lattice $\exp\left[i\vec{G}\vec{R}\right] = 1$ using the reciprocal lattice vector $\vec{G}$ and the Bravais lattice vector $\vec{R}$ directly yields the van-Laue condition [GM12]:

$$\vec{k'} - \vec{k} = \vec{G} \tag{2.8}$$

The van-Laue condition and therefore constructive interference for plane waves in 3-dimensional space is therefore affected by the reciprocal lattice vectors $\vec{G}$ for which momentum conservation holds [GM12]. The transition to constructive interference between parallel planes of the crystal lattice can be derived using the Van-Laue equation. Constructive interference of parallel planes can then be measured using X-ray diffraction (XRD) experiments. Since $\vec{G} = 2|\vec{k}|\sin[\vartheta]$ according to figure 2.9 and the minimal reciprocal vector which points from one parallel plane to the adjacent parallel plane is

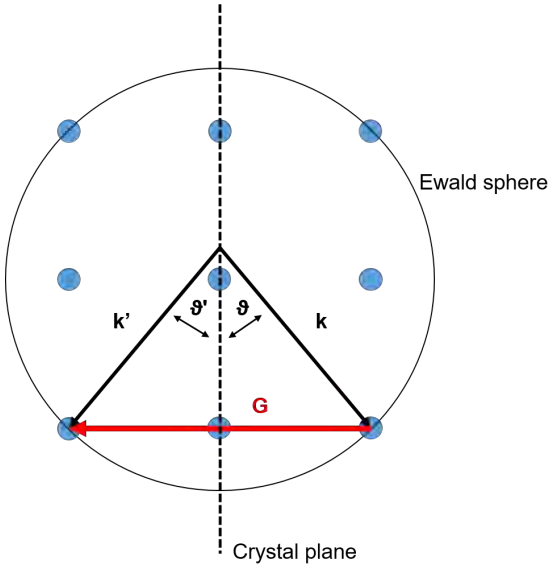

Figure 2.9: Ewald sphere: Construction of allowed k-k'-vector transitions according to momentum conservation in elastic scattering processes

$\vec{G}_m = \frac{2\pi}{d}\hat{G}_m$, we can thus conclude the famous Bragg law using $k = \frac{2\pi}{\lambda}$ [GM12]:

$$G = n \cdot G_m = n \cdot \frac{2\pi}{d} = 2\left(\frac{2\pi}{\lambda}\right)\sin[\vartheta] \tag{2.9}$$

$$n\lambda = 2d\sin[\vartheta] \tag{2.10}$$

Therefore, observed peaks at angles 2ϑ in XRD experiments are greatly dependent on the wavelength used.

2.4.4 Photonic structures

From Maxwell's equation

$$\nabla \times \vec{E} = -\frac{\mathrm{d}}{\mathrm{d}t}\vec{B} \tag{2.11}$$

one can deduce that the electric field $\vec{E}$ between two media must be continuous in surface-parallel projection. Neglecting absorption losses, the incoming light is being split at the interface into reflected and transmitted components. Using the unit vector $\vec{n}$ perpendicular to the interface, following equation must hold:

$$(\vec{E}_{tr} - (\vec{E}_{re} + \vec{E}_{in})) \times \vec{n} = 0 \tag{2.12}$$

With the trial of plane waves to solve the wave equation which can be deducted taking the rotation of equation 2.11, one can write the start with the following trial, featuring individual frequencies and k-vectors:

$$E_{\parallel,in} \exp\left[i(\vec{k_{in}}\vec{r} - \omega_{in}t)\right] + E_{\parallel,re} \exp\left[i(\vec{k_{re}}\vec{r} - \omega_{re}t)\right] = E_{\parallel,tr} \exp\left[i(\vec{k_{tr}}\vec{r} - \omega_{tr}t)\right] \quad (2.13)$$

Setting $\vec{r} = 0$ and $t = 0$, amplitudes must follow $E_{\parallel,in} + E_{\parallel,re} = E_{\parallel,tr}$. Varying t with fixed $\vec{r} = 0$, frequencies ω must be equal. Varying $\vec{r} = 0$ with fixed $t = 0$, the products $\vec{k}\vec{r}$ must be equal. Choosing $\vec{k_{in}}$ in the x-y plane without loss of generality, we can therefore conclude for the in-plane projection (x-z-plane): $k_{in,x}x = k_{re,x}x = k_{tr,x}x$. Using $|k_{in}| = |k_{re}|$ thus gives the law of reflection $\sin\alpha = \sin\alpha'$. The dispersion relation of photons which reads

$$k = \frac{\omega}{c} \cdot n \quad (2.14)$$

with speed c of light in vacuum and the refractive index n leads to the law of refraction:

$$\sin\left[\alpha\right] \cdot n_{in} = \sin\left[\beta\right] \cdot n_{tr} \quad (2.15)$$

Thus, it can be easily shown from equation 2.15 that a maximum angle for refraction exists:

$$\alpha_{\mathrm{TIR}} = \arcsin\left(\frac{n_{tr}}{n_{in}}\right) \quad (2.16)$$

Due to the photon's dispersion relation (equation 2.14) and the continuity of $\vec{E}_{\parallel}$, the parallel part of the $\vec{k}$-vectors must be continuous. A vizualization of total internal reflection is given in figure 2.10.

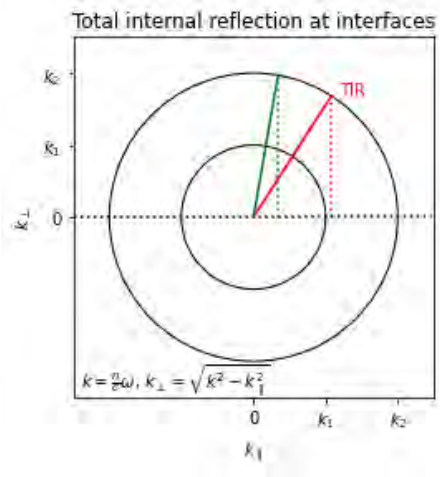

Figure 2.10: Total internal reflection depending on $k_\parallel$. Two materials (1) and (2) with $n_2 > n_1$ and a optical transition of material (2) to material (1). Green: Transmission of parts of the intensity from material (2) to material (1). Red: Angle of total internal reflection surpassed, no transmission.

2.4.5 Wave-guide modes, optical fiber

Wave-guiding inside an optical system happens as a consequence of the high refractive index difference between the wave-guiding (dielectric) material and the surrounding material. When a wave enters a wave-guide at high enough k-parallel values (perpendicular to the confining dimension), it is confined through total internal reflection. Confined modes in a wave-guide are then called wave-guide modes. In a 1D step-index wave-guide, take for example a high refractive index cuboid slab sandwiched between two layers of lower refractive index, we find one confining dimension [Sch16]. In such a 1D slab wave-guide, the confining dimension can be put at the x-direction and the direction of the propagating wave in the z-direction without loss of generality. Thus, one can start with a trial based on plane waves for both the magnetic and the electric field. Splitting p- and s-polarized modes, we can write [Sch16]:

$$\vec{E}(z,x,t) = \vec{E}_O(x) \cdot \exp\left[ik_z z - i\omega t\right]$$
$$\vec{H}(z,x,t) = \vec{H}_O(x) \cdot \exp\left[ik_z z - i\omega t\right]$$

The sum $\sum_{k_z}$ of these waves then leads to the spatial profile of the E-and H-field distribution. Employing this trial, waves have to satisfy the Maxwell equations. Amplitudes

of interfering waves traveling back and forth in the wave-guide can be found through continuity conditions at intersections between the core and the surrounding materials [Sch16]. One can see the comparability to solving a 1D or 2D quantum well problem. There are two main parameters which restrict or allow wave-guide modes to exist inside the wave-guide. The first is the confining dimension. There is a general trend to more allowed wave-guide modes with increasing thickness of the wave-guide. Further, the number of wave-guide modes is greatly dependent on the wavelength λ. More wave-guide modes are allowed for smaller wavelengths λ. Therefore, only a set of distinct wavelengths and k_{par} values (k-vector projection perpendicular to the confining dimension) allow for wave-guide modes inside the wave-guide, depending on the dimension and the dielectric function of the wave-guiding material [Sch16].
The SCIL-patterned perovskite layers discussed in this thesis can be seen as a step-index wave-guide with a confining dimension perpendicular to the layer interfaces, given by the thickness of the perovskite layer. The index difference between active layer and adjacent layers would thus yield $\Delta n = 2.2 - 1.56 = 0.64$ for the $MAPbBr_3$-PVK intersection and $\Delta n = 2.2 - 1.75 = 0.45$ for the $MAPbBr_3$-TPBi intersection. Using the hexagonal SiO_2 pattern inside the wave-guide, a periodic perturbation structure is embedded into the system. Therefore, a model for a periodic perturbation inside a wave-guide has to be found. Depending on the shape and periodicity of the pattern, this model must explain why specific in-plane k-vectors (k_x,k_y) are very prominent in the scattering image of PL whereas other sets of k-parallel components are not.
Periodic disturbance inside a wave-guide can be qualitatively modeled using an approach for wave-guide modes which inherits from the description of free-electron dispersion in periodic lattices in solid-state physics [Sch16]. Our SCIL-pattern is hexagonal. Due to the definition of reciprocal vectors $\vec{b}_i$ associated with a Bravais-lattice $\vec{a}_j$ which reads

$$\vec{b}_i \cdot \vec{a}_j = 2\pi \cdot \delta_{ij}$$

the reciprocal lattice of a hexagonal 2D structure resembles a hexagonal 2D structure itself [GM12]. With a pitch d between pillars of the periodic grid, dispersion is also periodic in reciprocal space with a shift of $G_m = \frac{2\pi}{d}$ from first Brillouin zone to first Brillouin zone. G_m being the minimal reciprocal space vector as explained in the upper section on the Van-Laue condition.
The dispersion relation for photons which propagate along the parallel axis inside the

wave-guide in vacuum reads:

$$E = \hbar \cdot k_{\text{par}} \cdot c$$

with c the speed of light in vacuum and k_{par} the k-vector projection in line with the pattern. In a non-perturbed wave-guide, meaning a perturbation structure inside the wave-guide which features the exact same real dielectric function n_p as the wave-guide material n_w, the band-structure of a 1D perturbation pattern is linear with increasing k_{par}. Consequently, no reflection occurs at the first Brillouin zone edges due to energy overlap. Figure (2.11, (a)) shows the 1D photon dispersion relation $E(k_{\text{par}})$ for the undisturbed case. Introducing a difference in dielectric functions between the wave-guide

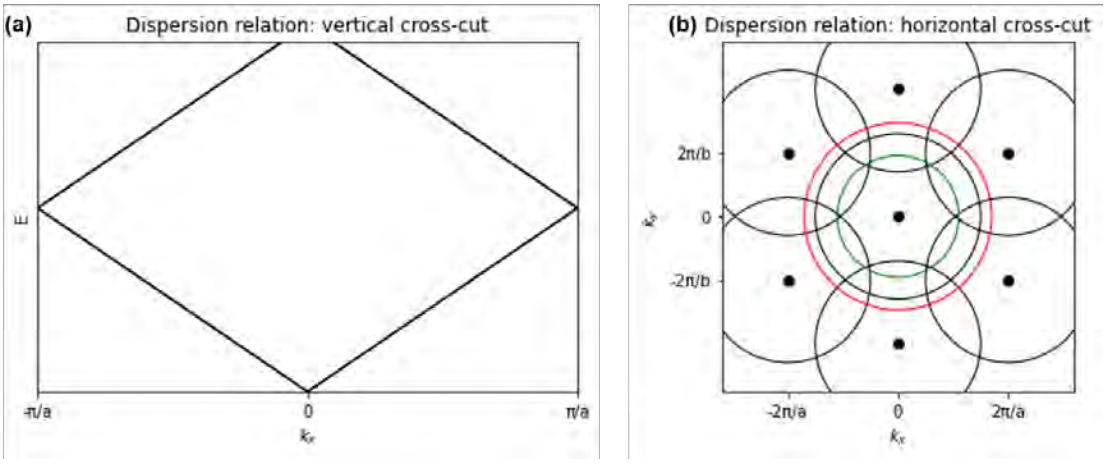

Figure 2.11:
(a): 1D dispersion relation of light: Linear $E(k_{\text{par}})$ relation with energy levels overlapping at the edge of the first Brillouin zone. Therefore, no reflection on the first Brillouin zone edge occurs ($k_{\text{par}} = \pm\frac{\pi}{d}$). Pitch d of the disturbance pattern.
(b): Horizontal dispersion cross-cuts of the 2D photon dispersion cones located at the reciprocal lattice points of the hexagonal pattern. The cross-cuts indicate iso-energy domains. The red and green circle indicates the k-parallel ranges of two objectives with different NA to show which k-parallel range can be portrayed.

material (n_w) and the periodic perturbation (n_p) (now $n_w \neq n_p$), band-bending occurs at the edge of the first Brillouin zone. Thus, we obtain an avoided crossing at the edge of the first Brillouin zone. As a consequence, Bragg-diffraction occurs as shown in the upper chapter according to the Laue-equation for k-parallel values of $k_{\text{par}} = \pm\frac{G_m}{2} = \frac{\pi}{d}$ [Sch16]. This happens due to the fact that only in-plane k-vectors survive inside the periodic perturbation which belong to constructively interfering waves [GBL+21]. Constructive

interference in periodic lattices is given by the Laue equation (equation 2.8). The $\vec{k}$-vectors associated with the Van-Laue condition are exactly the ones which point onto the Brillouin zone edge. Thus, the superposition of propagating waves inside the wave-guide leads to standing waves with the condition $\frac{\mathrm{d}E(k_{\mathrm{par}})}{\mathrm{d}k_{\mathrm{par}}} = 0$ at the Brillouin zone edges $k_{\mathrm{par}} = \pm\frac{\pi}{d}$ [GM12][Sch16].
Switching from the 1D to the 2D case, the free photon dispersion relation reads:

$$E = \hbar \cdot (k_{\mathrm{par,x}} + k_{\mathrm{par,y}}) \cdot c$$

When looking at the free 2D dispersion relation $E(k_x, k_y)$, it results in dispersion cones placed on the reciprocal lattice points with their symmetry axis in the direction of confinement of the wave-guide [Sch16]. To imagine these cones, we can start with the 1D dispersion relation shown in figure (2.11(a)) and rotate the picture around the vertical axis. The slope of these dispersion cones is proportional to the refractive index n, as $k = \frac{n\omega}{c}$.
When we take a horizontal cross-cut of these dispersion cones, therefore looking at the (k_x,k_y) dispersion from the top, we find iso-energy circles located on the reciprocal lattice points as indicated in figure (2.11, (b)). Every horizontal intersection of the light-cone represents an iso-energy $E_0(k_{x0}, k_{y0})$ domain, according to the photon's dispersion relation. Whereas the dispersion relation of the wave-guide modes scattered to far-field relates to free photon dispersion, the waves confined in the perturbation structure follow a more complex dispersion. Thus, we can see the free photon disperion as the upper limit for the in-plane k-vector distribution [GBL$^+$21]. When this horizontal intersection of the dispersion cone cuts the edge of the first Brillouin-zone (for example the M-or K symmetry point), the corresponding tuple (k_x, k_y) matches the Bragg-condition. That means that these intersections of iso-energy domain and Brillouin-zone edges determine the angular distribution of the modes inside the wave-guide [GBL$^+$21]. The corresponding waves interfere constructively in the system. Figure 2.12 shows the first and higher order Brillouin zones of the hexagonal lattice and the intersection of three circular dispersion cross-cuts which cut the Brillouin zone edges at distrinct points. By now, we have only taken the first Brillouin zone into account. This happened in direct comparison to the theory of electrons bond in solids. Since the photons inside the wave-guide can couple to far-field radiation as a consequence of scattering through the structure, the information on all wave-guide modes cannot be described by the first Brillouin zone only. Consequently, also higher order Brillouin zones have to be taken into account as shown in figure 2.12 [GBL$^+$21]. As a result of the overlap of the dispersion relation at a

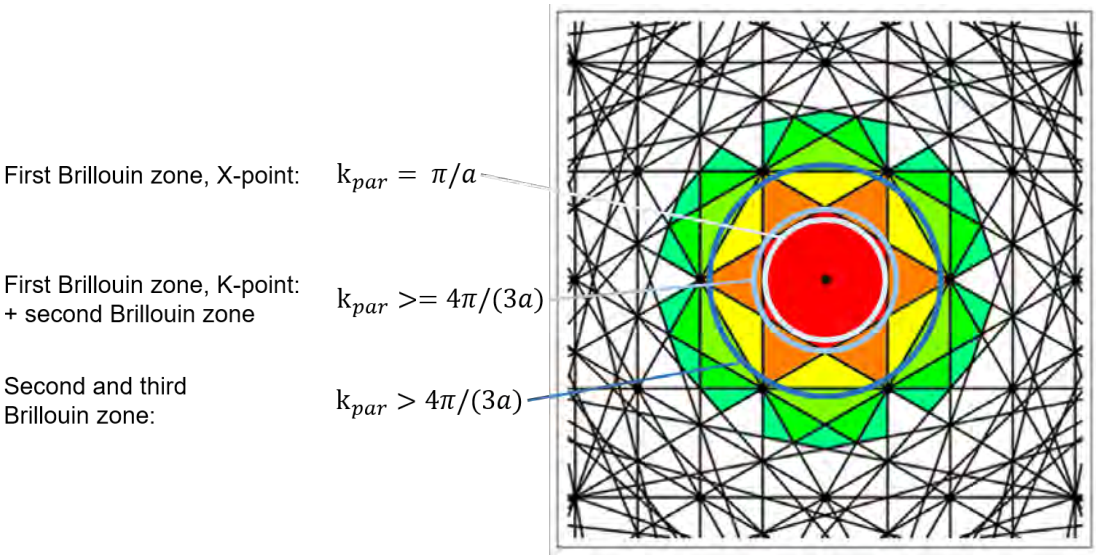

Figure 2.12: Brillouin-zones of hexagonal lattice: First (red), second (orange), third (yellow) and higher order Brillouin-zones are constructed.
Further, corresponding iso-energy circle of the dispersion light-cone is drawn for three different energies E as an example. Every cut of these circles with the Brillouin-zone boundaries corresponds to the Bragg-condition. The respective (k_x,k_y)-vectors are therefore constructively interfered within the lattice.

given energy E (circle) and the Brillouin zone edges, we can predict the spatial profile of the in-plane k-vector distribution measured in experiment for this specific energy E. By mapping all possible energies E_i with their iso-energy circle to the Brillouin-zone edges, we can further predict the in-plane k-space distribution for a set of energies E_i [GBL+21].

As we have already seen, the two crucial parameters which allow or forbid wave-guide modes are the thickness and the wavelength λ. With the knowledge gained on periodic perturbations, more parameters come into play.

At first, there is the energy distribution ΔE. If only one specific energy E_0 is confined in the wave-guide, we see single dots in the k-space distribution [GBL+21]. This is due to the intersection of only one single dispersion cross-cut (circle) at E_0 with the Brillouin-zone edges. Take for example the innermost circle in figure 2.12 which translates to the M-symmetry point of the first Brillouin zone of the hexagonal reciprocal lattice. This would result in six points, ordered in a hexagon. If we have a range of energies $\Delta E = E_1 - E_0$, the k-space distribution of scattered modes starts at the intersection of the dispersion cross-cut of E_0 with the Brillouin zone edges and ends at the intersection related to E_1. One has to mention that this argumentation is based on the free-photon

dispersion. As the waves are in reality confined in the periodic structure, their photon dispersion is somewhat more complicated and dense. Thus, energy E is not necessarily proportional to the k-parallel component [Sch16] [GBL+21]. Yet, the free-photon dispersion relation serves as an upper limit for the maximal in-plane k-vector corresponding to an energy E. The intensity distribution in plane k-space is determined by the high-symmetry points within the Brillouin zones [GBL+21]. One could also speculate about how the intensity distribution ΔE of the PL spectrum affects the in-plane k-space distribution.
A second parameter which changes the k-space distribution clearly is the pitch d of the periodic perturbation structure. If only one energy E_0 existed in the system with its corresponding dispersion cross-cut (circle), it intersects at given Brillouin zone boundaries as shown in figure 2.12. These Brillouin zone boundaries are determined by the pitch d. If the pitch d in real space is now increased from d to d_1, the Brillouin zones shrink as the lowest reciprocal vector G_m equals $\frac{2\pi}{d_1}$. Thus, the scattering image is shifted towards higher Brillouin zones. This means that the Bragg-condition of the exact same wavelength λ_0, which corresponds to E_0, is now matched in a higher Brillouin-zone. Thus when the pitch d is increased, directionality of predicted in-plane k-space distributions of scattered wave-guide modes is determined by higher order Brillouin-zone edges and vice versa. The distribution in k-space is still dotted due to the assumption of only one single energy E_0 [GBL+21].
The width b or height h of the pillars in the perturbation pattern should change the scattering intensity, yet the in-plane k-space distribution of the scattered light should remain as the pitch d and the energy distribution ΔE are not changed.
When the perovskite material is changed, it PL spectrum is located at different wavelengths $\Delta lambda$. Given that wave-guide modes are still allowed in the perovskite layer, a change to higher wavelengths λ would shift the in-plane k-space distribution towards lower order Brillouin zone edges due to $k = \frac{2\pi}{\lambda}$.

By adding a periodic perturbation into the wave-guide, trapped light in the form of wave-guide modes can be scattered from the near-field to the far-field and thus can be visualized using back-focal plane imaging. The in-plane k-space distribution is dictated by the periodic structure (pitch d) and the energy distribution ΔE. The numerical aperture NA of the objective restricts the range of (k_x, k_y)-values by $k_{\mathrm{x,max}} = k \cdot \mathrm{NA}$. The circle of k-parallel values which can be portrayed by the objective are sketched for two different NAs (green and red circle) in figure (2.11, (b)). Since we use a 534nm long pass filter in the experiments, the highest photon energy corresponds to $\lambda \approx 540$nm. In

combination with an objective which features a numerical aperture of NA = 0.85, we find $k_{\mathrm{x,max}} = 0.85 \cdot \frac{2\pi}{540\mathrm{nm}}$ as the maximum k-parallel vector in our experiments.

3 Experimental methods and materials

3.1 SCIL: Substrate Conformal Imprinting Lithography

In this work, structuring of $MAPbBr_3$ is based on substrate conformal imprinting lithography (SCIL). SCIL is a nano-imprinting lithography technique which combines advantages of both soft and rigid stamps. Thus, high resolution and uniformity of rigid stamps is paired with conformal contacting between stamp and material surfaces reserved to soft stamps. SCIL can therefore produce sub 10nm patterning structures with remarkable surface coverage. Secondly, SCIL prevents damaging the cured, imprinted pattern when releasing the stamp due to the soft rubber materials used. Whereas rigid stamps are likely to damage the cured pattern when releasing caused by shearing forces, soft stamps lack uniformity in imprinting patterns due to their low Young's modulus. Both of these main issues can be overcome using SCIL [VMN+17].
The stamp's technical implementation is based on soft silicone rubber materials such as PDMS (poly-dimethyl-siloxane) which are attached to rigid glass sheets [VMN+17]. Choosing a Young's Modulus for the PDMS materials which provides a balance between flexibility and rigidity and combining stiffer X-PDMS and softer low modulus rubbers, high adaptability of the stamp's dimensions, dependent on the flatness of the surface which is imprinted, can be achieved. To avoid defects in the patterned structure when applying and releasing the stamp which can occur due to in-plane shearing forces which stretch the flexible PDMS material, the PDMS stamp is backed by a thin, bendable sheet of glass [VMN+17]. Therefore, good surface coverage by out-of-plane bending and the softness of the stamp can be achieved while restricting deformations of the stamp regarding in-plane shearing forces. The stamp's pattern thus stays intact over large areas. These PDMS-stamps themselves were fabricated by a rigid master stamp, molding liquid PDMS into the inverse pattern of the master through physical connection [VMN+17]. The SCIL stamp based on PDMS material is shown in figure 3.1.

3.1.1 SCIL: Imprinting process for patterned $MAPbBr_3$ layers

The samples in this work feature 1.5cm x 1.5cm dimensions, thus the SCIL imprinting process is conducted manually by hand. For wafer-sized samples, one might opt for

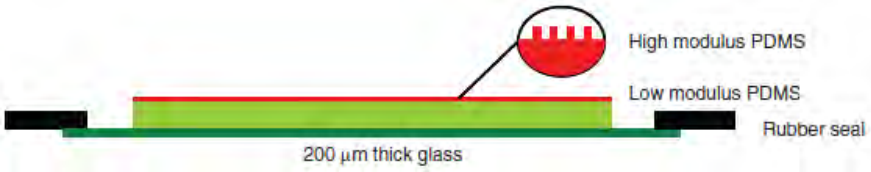

Figure 3.1: SCIL stamp based on PDMS silicone rubber applied on glass. With SCIL, rigid glass and soft PDMS-rubber together combine advantages of rigid and soft stamps used for nano-lithography. Graph by [VMN+17]

machine-controlled application of the SCIL stamp.
Due to the stamp's out-of-plane flexibility which is crucial for good surface coverage, it was bent in a U-shape and then first applied onto the center of the substrate. When in visible connection with the stamp at the contact point, aided by capillary forces filling the stamp's pattern with liquid sol-gel, the U-bending of the stamp was slowly and evenly released to both sides. Without applying additional mechanical pressure, full surface coverage of the stamp could be achieved by capillary forces only. Releasing the bend of the stamp slowly lead to very little entrapment of air between stamp and substrate. This is also due to the fact that PDMS features high permeability for gases [VMN+17]. After a time of 6min in which the silica-based sol-gel resist cures under ambient conditions (no additional illumination needed), the stamp is turned around and the sample released by slowly bending the stamp away from the sample.

3.2 LED stack architecture: SCIL-patterned and non-patterned

This work uses a common perovskite LED stack for green emission (λ = 535nm) and introduces SCIL lithography on it (figure 3.2). To proof the concept of distinct wave-guide mode scattering out of perovskite layers using an imprinted structure, both SCIL-patterned as well as non-patterned versions of this stack are investigated under the Fourier microscope. As this whole thesis is based on a comparative style of analysis, the main goal is maximum comparability of the patterned and the non-patterned stack. Only if high comparability is achieved, it is possible to directly deduct observed effects to the patterning. As will be explained in the fabrication section below, the $MAPbBr_3$ layer itself added the most variance between samples due to its moderate reproducibility. In order to eradicate the variance of the perovskite layer between samples, substrates are imprinted on one half and processed as flat on the other half of the same substrate. This is shown in figure 3.2. Thus, experiments can be conducted on the exact same sample which rises comparability. Differences in crystallization, lifetime and absorption of pat-

terned and flat perovskite layers which might occur due to the SCIL-structure inside the perovskite layer can thus easier be attributed to the patterning itself. Further stacks are

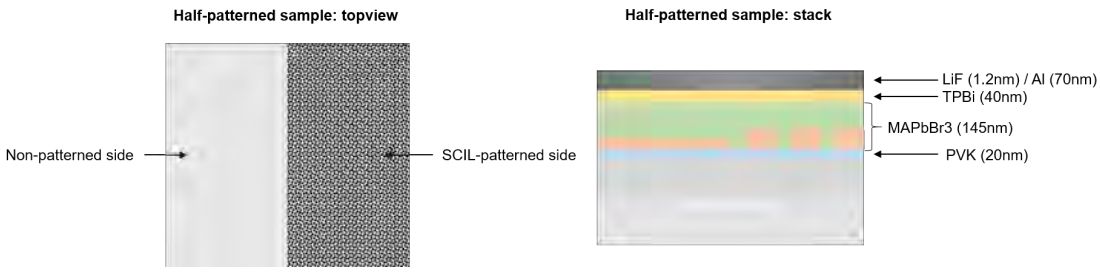

Figure 3.2: Complete stack investigated under the Fourier-microscope to proof distinct wave-guide mode scattering

analyzed in experiment as shown in figure 3.3. As these stacks are less complicated in their electronic structure compared to the complete stack, they back up the findings on the complete stack (figure 3.2) and results are easier to attribute to the SCIL-structure directly. As depicted in figures 3.2 and 3.3, patterning the sample only on one half of

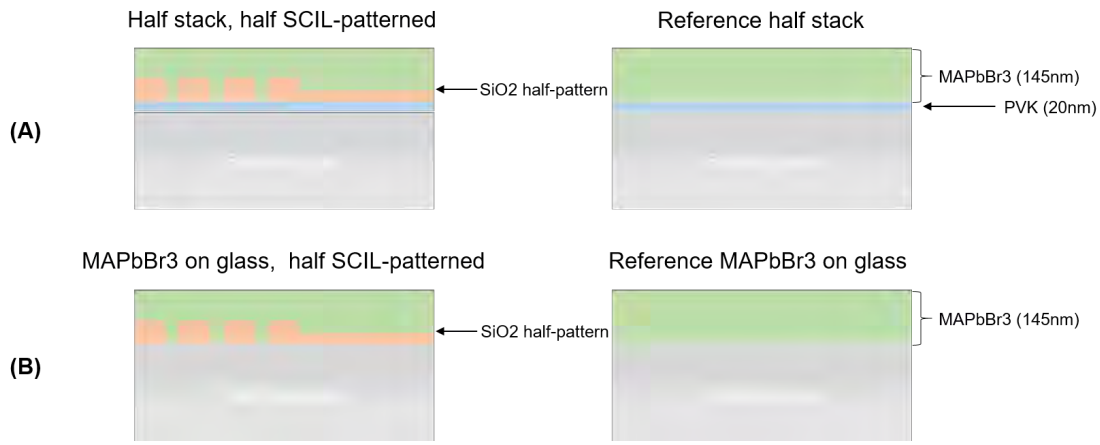

Figure 3.3: $MAPbBr_3$ stacks used to determine the opto-electronic properties of the SCIL-patterned perovskite layers.

the substrate's surface leads to a residual SiO_2 layer on the non-patterned side. Thus, the differences between the patterned and flat side that are observed might not only result from an effect of the patterning, but also from insulating the perovskite layer from the underlying PVK layer or the glass surface. For this reason, the compulsory measurements conducted on half-patterned samples are compared to a reference sample as shown in figure 3.3. Thus, differences between the flat and patterned side of the half-patterned sample can be measured (eradicating perovskite variance) and are then

validated by flat reference samples. From this information, conclusions on direct effects of the pattern can be drawn.
Note that ITO (which acts as a transparent electrode in a regular perovskite LED) is not present in figure 3.2 due to special requirements in the Fourier-microscope which was used for k-space resolved PL imaging. However, we believe that the absence of ITO does not have a decisive effect on the proof of concept this thesis provides regarding PL waveguide mode scattering out of perovskite LEDs. It is assumed that for photo-luminescence measurements, band interfaces of the carrier transport layers to the perovskite layer are more critical for the performance of the stack under illumination.
Among several other factors for efficent p-i-n hetero-structures under operation, proper band alignment for carrier injection and carrier blocking plays a crucial role as explained in the theory section. The particular band alignment of this green emissive stack is shown in figure 3.4.

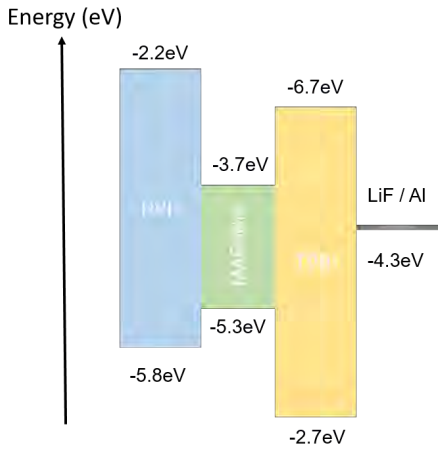

Figure 3.4: Lowest conduction band and highest valence band plotted for every material used in the full stack shown in figure 3.2; [TZL+20] [ALM10] [ZWP+17]

3.3 Fabrication: SCIL-patterned and non-patterned

3.3.1 Fabrication process

The perovskite LED stacks were fabricated based on the architecture shown in figure 3.2. Fabricating these stacks from bottom to top, layer by layer is spin-coated or evaporated onto the borofloat glass substrate which features common 1.5cm x 1.5cm dimensions. The process is shown in figure 3.5. The borofloat glass substrates were IPA wiped, then brushed with soap and water to remove a polymer coating. A following 20min sonication

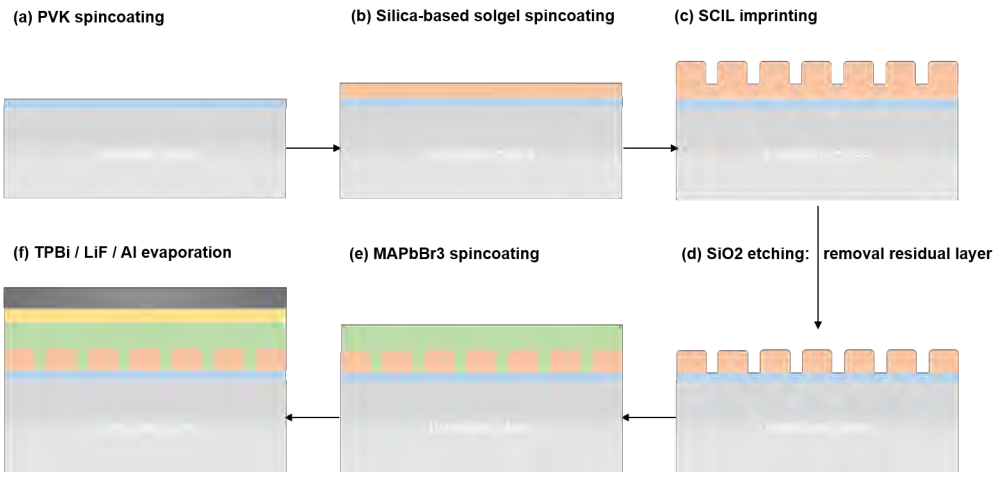

Figure 3.5: Fabrication process in six steps

in demi water, acetone and finally IPA served to clear any remaining polymer and traces off the sample. Right before application of the PVK layer deposited using spin-coating, the sample was O_2-plasma cleaned for 30 seconds (Oxford Instruments Plasma 80, 50W forward power, pressure $p < 10^{-6}$mTorr) in order to activate the glass surface. Powdery PVK was dissolved in chlorobenzene at a 15mg/ml concentration. Applying 3 drops of PVK-solution through a 0.45μm filter, PVK was then spin-coated for 45 seconds at 2000rpm with 1000rpm/s acceleration and subsequently annealed for 20min at 120°C under ambient atmosphere. As a second step, silica-based sol-gel was taken out of the freezer (-18°C) 30min prior to spin-coating. It was then applied onto the sample using 3 drops of sol-gel solution through a 0.2μm filter under ambient atmosphere. After spin-coating silica-based sol-gel for 8 seconds at 2000 rpm with 2000rpm/s acceleration, the SCIL-PDMS stamp was directly applied onto the wet sol-gel for 6min before being released again. Read for detailed description of the SCIL-stamping procedure in the SCIL-section below. The hardened SiO_2 pattern was then etched for 2:30min in CHF_3-Ar plasma to remove the residual layer of the pattern (Oxford Instruments Plasma 80, 100W forward power, pressure $p < 10^{-6}$mTorr). Thus, the $MAPbBr_3$ layer which was subsequently spin-coated on top of the etched SiO_2 pattern could electrically contact the underlying PVK layer. Concerning $MAPbBr_3$ deposition, the surfaces of the etched-through SiO_2 pattern as well as the underlying PVK layer were activated through another 30s O_2 plasma descum. Thereafter, a 0.5M solution of $MAPbBr_3$ dissolved in a 4:1(v:v) DMF:DMSO ratio was spin-coated using the solution-exchange technique under nitrogen atmosphere. 100μl of 0.5M $MAPbBr_3$ solution were applied onto the sample

through a pipette and then spin-coated at 4500rpm with 4500rpm/s acceleration for 30 seconds. In a solution-exchange process, 200μl of chloroform where added onto the spinning sample 10 seconds after starting the spin-coating procedure. Samples were subsequently annealed at 100°C for 15min. The remaining TPBi layer which serves as an EIL and the LiF/Al electrode were finally evaporated onto the sample (Angstrom Engineering thermal evaporator).

3.3.2 Challenges in fabrication: SCIL-patterning and perovskite layer deposition

The fundamental requirement in fabricating non-patterned and SCIL-patterned samples is comparability in analysis. Since the SCIL-patterned samples do inherit more steps than the non-patterned ones during fabrication, layers might not all be treated exactly the same in both the structured and flat stack. This might lead to different surface morphologies and therefore differing layer interfaces. Further, differences in fabrication also effect layer thicknesses (every descumming process takes away a certain height of the layer in contact with the O_2 plasma) and thicknesses might thus differ between the structured and unstructured sample.
For this reason, every descumming procedure and etching step used for SCIL-imprinting is also conducted in the fabrication process of the non-patterned sample. Doing this, it is ensured that layer thicknesses stay comparable and that changes in surface morphology due to descumming are present in both types of samples. Still, as spin-coating on a patterned SiO_2 surface leads to higher perovskite layer thicknesses compared to the flat case, all results in analysis are being discussed with respect to the difference in volume between the active layers of both samples.
The most important challenge for comparability of SCIL-patterned samples and flat samples proved to be the reproducibility of the perovskite $MAPbBr_3$ layer. Intriguingly, reproducibility of the SCIL pattern turned out to be very decent. Since spin-coating $MAPbBr_3$ solution on structured surfaces changed the visual appearance of the resulting $MAPbBr_3$ layers greatly (cracks, haze) when spin-coating at speeds <4000rpm and at molar concentrations of >0.5M, a reproducible perovskite spin-coating recipe which works equally well on both flat and patterned structures was finally found in a 0.5M $MAPbBr_3$ precursor solution (diluted in 4:1 DMF:DMSO (v:v)) spin-coated at 4500rpm. Lower molarities <0.5M did not provide the required height of the active layer to achieve full coverage of the underlying SCIL pattern. Recipes were deducted from findings by Rand et al. ([KZXR16]).
Layer thicknesses of the PVK layer were measured using a profilometer (KLA Tencor Stylus Profiler P7). To serve the requirement of comparibility between both stacks, the

initial thickness of PVK after spin-coating must be high enough in order to withstand the number of O_2 plasma activations needed until the desired layer thickness of 20nm is reached. Using the profilometer, the thickness decrease of PVK in every 30 seconds O_2 descumming process was measured to be $\approx$ 5nm. The etching process through the residual SiO_2 pattern was validated by SEM cross section imaging in order to find the correct etching time for a fixed CHF_3-Ar etching recipe which removes the residual layer of the SCIL pattern completely.
Lastly, the quality of the SCIL imprint depends greatly on the freshness of the silica-based sol-gel used as the resist and further, it also depends on the surface activation process (O_2 descum). Therefore, O_2 descumming should be conducted right before sol-gel application. It is recommended to descum all samples one by one and using a sol-gel not older than 1h. Otherwise, the silica-based solgel solution might have gelated to an extend at which its viscosity prevents the sol-gel from being attracted into the stamp pattern. In addition, the spin-coating process of wet sol-gel should be as short as possible and the stamp be applied as quickly as possible after in order to prevent the sol-gel from drying to an unprintable state.
The filling of the pattern by the spin-coated $MAPbBr_3$ layers turned out to be very reproducible (figures 3.6 and 3.7) even for different molarities M of perovskite precursor solutions. The main issue was posed by differences in visible haze and cracking between the patterned and the non-patterned perovskite layers which was enventually overcome using the 0.5M $MAPBBr_3$ solution (DMF:DMSO 4:1 (v:v)) spin-coated at 4500rpm in a solution-exchange process with chloroform.

3.3.3 Results of SCIL-pattern fabrication

SEM images were taken to proof the homogeneity and uniformity of the structures of the SCIL pattern. In figure 3.6 on the left, a cross-section of a PVK layer with an etched-through SiO_2 pattern on top is shown . Figure 3.6 shows the uniformity in shape and height of the SiO_2 pillars. To proof that this pattern shows high homogeneity over larger areas, the right picture in figure 3.6 presents a top view of the SCIL-imprinted SiO_2 after the etching process of the residual layer over a μm-range. As can be seen in figure 3.6, the underlying PVK layer is still intact even after the CHF_3-Ar plasma etching step. The selectivity of the CHF_3-Ar etching process which etches the SiO_2 residual layer of the pattern but does not etch the PVK layer was found by co-workers of Albert Polman at AMOLF Amsterdam. Thus, finding a selective etching process is greatly important when the pattern is deposited between the HIL and the active layer as in this thesis. It might be easier for further application to SCIL-pattern the ITO layer directly, thus

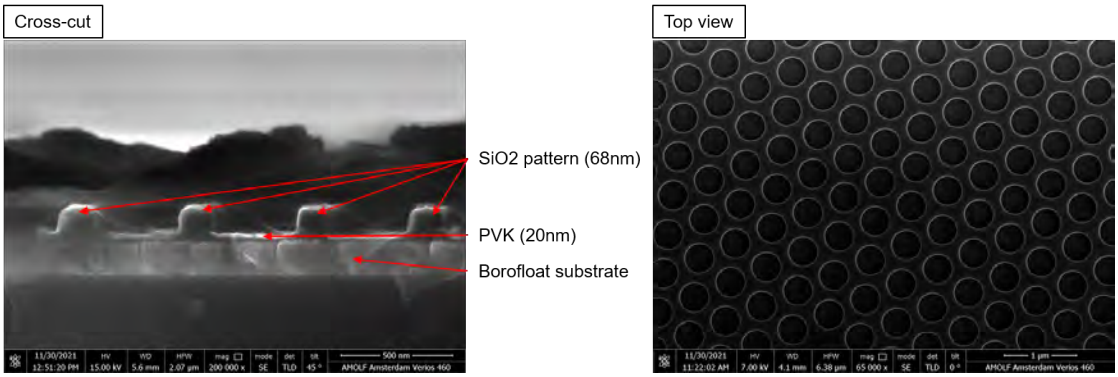

Figure 3.6: SEM cross-section of SCIL-patterned SiO_2 and underlying PVK after CHF_3-Ar etching: The cross-section proves uniformity of pillar height and integrity of underlying PVK layer after SiO_2 etching. SEM top view: Shows homogeneity of patterning over larger μm scales

patterning both the HIL and perovskite layer.

Spin-coating a perovskite layer on top of this SiO_2-structure, a SEM cross-cut of this fabrication step is shown in figure 3.7. Figure 3.7 shows proper filling of $MAPbBr_3$ in

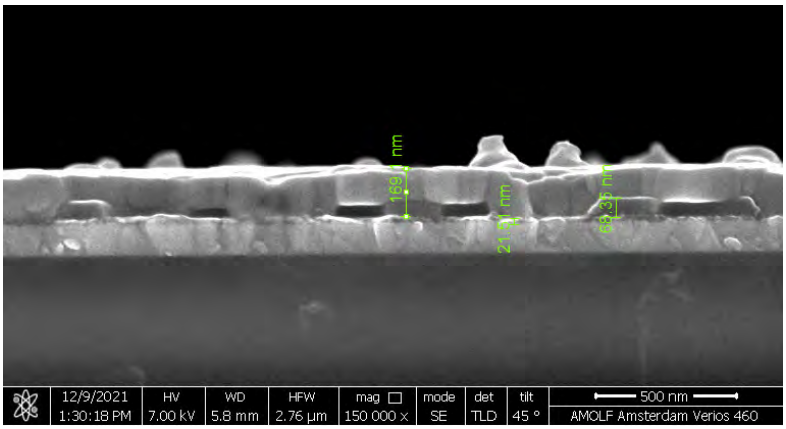

Figure 3.7: SEM cross-section. 0.5M precursor solution of $MAPbBr_3$: Borofloat glass with PVK layer (21.5nm), SiO_2 pattern (69.35nm) and a $MAPbBr_3$ (169nm). Grain boundaries in the $MAPbBr_3$ layer visible, SiO_2 pillars are uniform in height and shape, $MAPbBr_3$ fills space in between the pillars.

between the pattern. Grain boundaries are clearly visible in figure 3.7, yet the perovskite-air surface is not very flat due to the low layer height. Still, this does not pose a problem for sharp PL scattering of wave-guide modes as will be shown in the analysis section.

3.4 Experimental methods

3.4.1 Fourier plane optical microscopy: Back-focal plane imaging

Fourier plane optical microscopy depicts the in-plane k-vector distribution k_x and k_y (optical axis z) of light emission and scattering by imaging the back-focal plane of the objective [Ro0]. Thus, the directionality of scattered wave-guide modes out of the SCIL-patterned perovskite layer can be measured.

The functioning principle of back-focal plane imaging to portray an in-plane k-space intensity distribution is based on diffraction theory. As the (Fraunhofer) diffraction pattern $E(k_x, k_y)$ of a plane aperture is proportional to the two-dimensional Fourier transformation of its opening function $\Omega_A(\xi, \nu)$, meaning $E(k_x, k_y) \propto \int_{\Omega_\nu} \int_{\Omega_\xi} \Omega_A(\xi, \nu) \cdot \frac{\exp[ikr]}{r} \mathrm{d}\nu \mathrm{d}\xi$, the diffraction pattern can be brought from infinity to considerable distances using a lens [ZZ18]. When a lens is installed at the focal distance f to the aperture, light rays which propagate in the same direction (k_x, k_y) are in approximation focused on the same spot at the back-focal plane, therefore being transformed into the aperture's far-field diffraction pattern [Hec18] (figure 3.8). As a second step, we can also re-transform the k-space distribution back to its real space distribution. To understand this, we assume that the k-space distribution which is focused at the back-focal plane of the first objective serves itself as an illumination source at this very plane. Thus, setting up another lens in the distance 2f to the first lens, the k-space image is re-transformed into its real space image [Hec18].

A common implementation of the Fourier-microscope using three lenses is shown in the following:

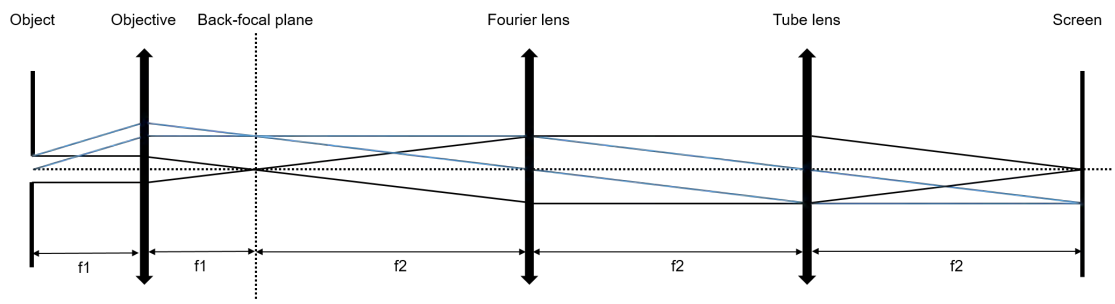

Figure 3.8: Implementation of a Fourier microscope for back-focal plane imaging. A k-space image is taken using the Fourier lens. A real-space image can be acquired without the Fourier lens, thus transforming the system into a real-space microscope.

In the fourier-setup used in this thesis, a 2kHz 534nm laser is coupled into the system

from the same side as the photo-luminescence of the perovskite layer is taken. To prevent imaging laser light, a 534nm low-pass filter is applied. It is clear that illumination of the sample with a 534nm laser is not ideal due to the fact that the maximum of the $MAPbBr_3$ PL spectrum is at $\lambda_{max} = 534$nm. Thus, the lowest wavelength of the spectrum which is transferred through the filter in this setup is $\lambda = 540$nm, lower wavelengths λ are cut off. Intriguingly, the k-space resolved scattering measurements still show sharp details which proves that for $\lambda \geq 540$nm, we still find wave-guide modes and sufficient scattering characteristics in the system. In order to obtain a proper signal-to-noise ratio, counts are integrated over a time of 250ms.

3.4.2 TCSPC: time-correlated single-photon counting

A detailed description on PL and the modeling behind the TCSPC (time-correlated single photon counting) measurement was already given in the theory section. Now, we focus on the experimental setup behind the TCSPC measurement. Measuring the transient PL decay, a pulsed layer excites the material at a given repetition rate γ. Between excitation, the excited carrier concentrations n and p recombine in radiative and non-radiative fashion. It is thus important to time the repetition rate γ to the point that PL can always decay (decay time τ) to noise level: $\gamma < \tau^{-1}$. Otherwise, build-up effects in PL might occur over time [KMSU20]. A scheme of the TCSPC setup is given in figure 3.9. In this thesis, a 485nm CW laser is used with a power on the spot of 0.94μW.

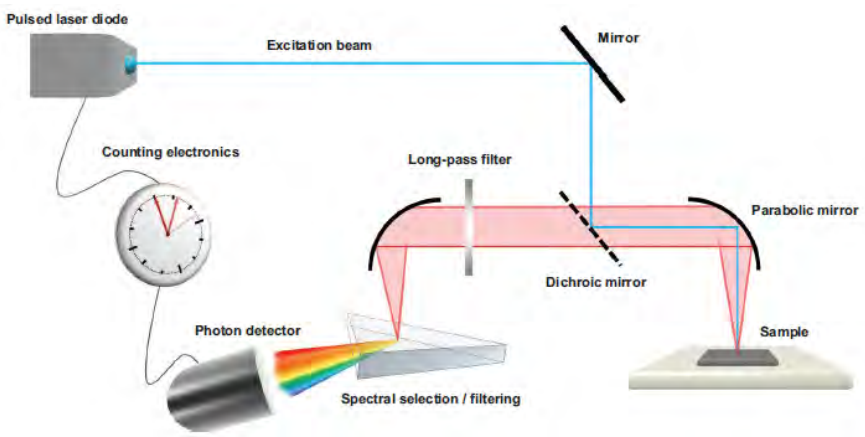

Figure 3.9: Setup TCSPC measurement: A pulsed laser excites the sample (repetition rate r), PL emission is then detected by a photo-multiplier or avalanche photo-detector (APD). Excitation and detection are timed to correlate PL signal and laser pulse. Graph by [KMSU20]

We use a cycle duration of 120ns for the repeating laser pulse as the PL properly decays

to noise level within this time.

3.4.3 X-ray diffraction (XRD)

Structural analysis using X-ray diffraction (XRD) provides insights into crystallization of materials. Dependent on symmetries of the crystal lattice, constructive and destructive interference of photons between adjacent crystal planes can be measured. The underlying physics are given by the Van-Laue-condition (equation 2.8), from which Bragg's law can be deducted (equation 2.10).
With XRD in general, differences in crystallization can be identified. Conclusions can be drawn both from absolute count values and relative intensity of the peaks with special focus on relative intensity since this will provide insights into the composition of the basis of the lattice. In addition, one can conclude differences regarding crystal growth parallel to the substrate [GM12].
Using a 0.5mm knife in the measurements, XRD scans can be deducted with proper spatial accuracy on both the SCIL-patterned and the flat side of the same sample which is shown in figure 3.3. XRD measurements were measured at a step-size of $\Delta(2\Theta) = 0.02°$ on a range of $2\Theta = 2° - 65°$ under a 1s integration time. Owing to the cubic conventional cell (compare figure 2.1) of the $MAPbBr_3$ lattice featuring (100), (200),...(n00) planes, the angular range was chosen to capture peaks up to the (400) plane since the angles of the (n00) planes in bulk $MAPbBr_3$ are given as follows for $\lambda = 15.41$nm: $2\Theta_{(n00)} = n \cdot 15°$.

3.4.4 UV-vis

UV-vis steady state absorption measurements can be used to calculate the optical band-gap E_G of the (perovskite) material investigated upon measured absorption A. It is specifically interesting if absorption A and potentially also the band-gap E_G can be changed by patterning.
Using an integrating sphere in a LAMBDA 750 UV/Vis/NIR spectro-photometer (perkin elmer), the fraction of absorbed light A can be calculated using $T + R + A = 1$ with the fraction of reflected light R and the fraction of transmitted light T[PI].
The so-called Tauc plot with which one can fit the absorption edge and therefore calculate an estimate for the band-gap E_G can be deducted from Lambert Beer's law

$$I(l) = I_0 \cdot \exp -\tau l \tag{3.1}$$

with the incident intensity of monochromatic light I_0, the path length l through the sample and the extinction coefficient τ. Thus, $A = \frac{I}{I_0}$. The Tauc plot is then fitted

plotting $(\tau h\nu)^{1/p}$ over the photon energy $h\nu$ which holds when we assume that the extinction coefficient τ is dependent on the band-gap energy E_G in the following way [MPM18]:

$$(\tau h\nu)^{1/p} = C \cdot (h\nu - E_G) \tag{3.2}$$

Here, $p = 1/2$ holds for direct band-gaps which is the case for $MAPbBr_3$. Solving equation 3.1 for $(\tau h\nu)^{1/p}$ therefore yields:

$$(\tau h\nu)^2 = (\frac{\ln(A^{-1})}{l} h\nu)^2 \tag{3.3}$$

The dependence on l is not relevant for the position and angle of the linear part of the tauc plot[Rig21].
The absorption scans are measured over a wave-length range of $250-800$nm as we expect the absorption edge of $MAPbBr_3$ to be at ≈ 530nm (2.34eV).

4 Analysis

4.1 K-space resolved photo-luminescence analysis: Wave-guide mode scattering

To prove the concept of distinct wave-guide mode scattering out of patterned $MAPbBr_3$ layers, different perovskite stacks are investigated under the Fourier microscope, imaging the back-focal plane of the objective. This gives the in-plane k-space intensity distribution of the wave-guide modes scattered to the far-field. The in-plane k-space distribution of the flat perovskite layer as well as the SCIL-patterned perovskite layer are measured on the same sample.

Starting with a $MAPbBr_3$ layer on glass only, the in-plane k-space intensity distributions of both a SCIL-structured $MAPbBr_3$ layer as well as a flat $MAPbBr_3$ layer are shown in figure 4.1. Both distributions are equaled in the intensity scale for comparison reasons. When both in-plane k-space distributions in figure 4.1 are compared, intensities for low angles ($\frac{k_x}{k_0} < 0.3$) are somewhat equal between the flat and the structured sample. Now looking at larger angles ($\frac{k_x}{k_0} > 0.3$), sharp scattering patterns are visible only for the SCIL-structured perovskite sample. We can thus interpret the in-plane k-space distribution of the SCIL-patterned perovskite layer as the overlay of two different intensity distributions: At first, there is the in-plane k-space distribution of the non-patterned per-

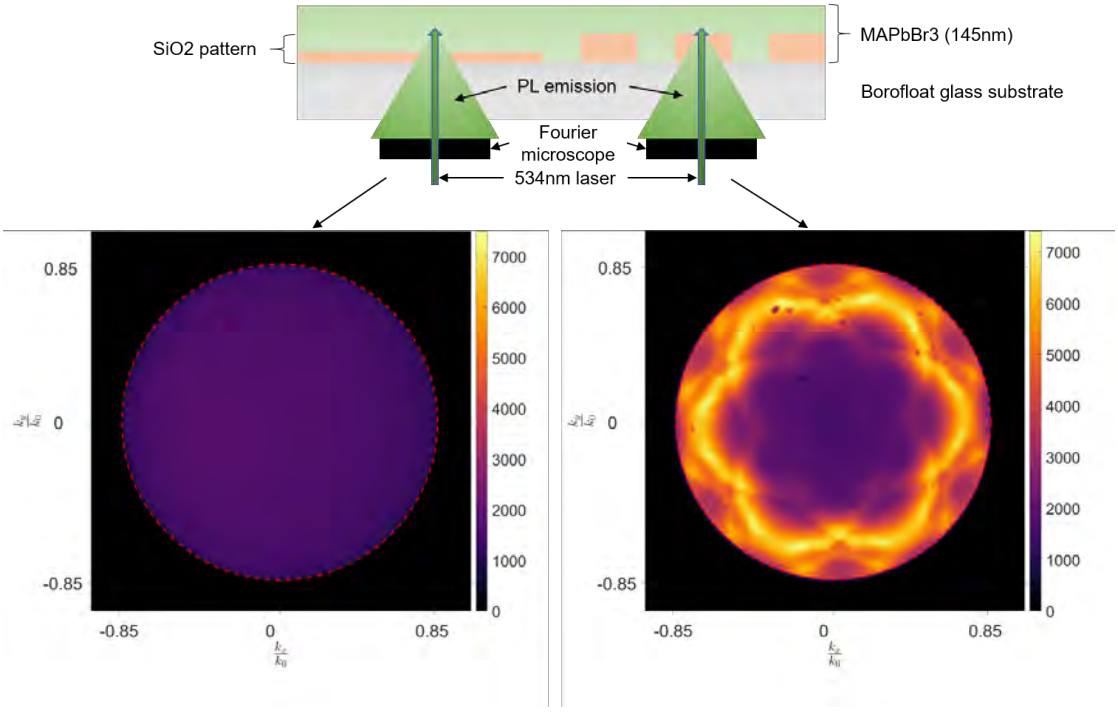

Figure 4.1: In-plane k-space distribution $(\frac{k_x}{k_0}, \frac{k_y}{k_0})$ of SCIL-patterned (right side) and non-patterned (left side) $MAPbBr_3$ on borofloat glass. Numerical aperture of objective: NA = 0.85. Distinct scattering pattern visible for the SCIL-structured active layer, non-structured layer with more homogeneous scattering.

ovskite layer. This distribution is not attributed to wave-guide mode scattering. Rather, it represents the intensity distribution radiated by a quasi Lambertian scatterer (perovskite). Secondly, the base-line intensity distribution of the non-patterned $MAPbBr_3$ is superpositioned by a sharp in-plane k-space distribution. This sharp distribution can be attributed to wave-guide mode scattering.

Interpreting the intensity distribution of the SCIL-patterned perovskite layer in figure 4.1 as a superposition of a Lambertian baseline and a distrinct wave-guide scattering image, it is obvious that light-outcoupling is heavily improved over the non-structured sample. To quantify this light-outcoupling effect which is caused by wave-guide scattering, the PL spectrum in figure 4.2 gives a factor of ≈ 2 for the intensity increase at the peak of the spectrum ($\lambda = 540$nm) between structured and non-structured sample. We cannot quantify the light-outcoupling improvements over the whole spectrum since the spectrum is cut off in experiment by the 534nm filter. But as the spectrum should follow a normal distribution with a peak at $\lambda \approx 530 - 535$nm, the improvements in light-outcoupling should be visible over the whole spectrum. Findings by [MLT18]

also suggest that the amount of wave-guide scattering is somewhat independent of the wavelength λ in the visible spectrum for one and the same pattern.

For the non-patterned in-plane k-space intensity distribution (figure 4.1, left picture), we observe intensity $I \neq 0$ up to $k_x = 0.85$ which is the limit of the objective. Since $k_x = 0.85k$ corresponds to an incident angle of $\alpha = 58.21°$ and yet the edge of total internal reflection is $\alpha_{\text{max}} \approx 42°$ (equation 2.16) for both the perovskite-glass and the glass-air interface, it shows that this broad intensity distribution results from the widening of the escape cone at each interface, transferring from $n_{\text{pero}} \approx 2.2$ to $n_{\text{glass}} \approx 1.5$ to $n_{\text{air}} = 1$.
Now looking at the interpretation of the sharp in-plane k-space intensity distribution of the SCIL-pattern in figure (4.1, right picture), a symmetric distribution is obtained. Thus, emitter-dipole orientation should be randomly distributed inside the system. Both the peak width $\Delta\lambda$ of the PL emission spectrum which accounts for an energy distribution ΔE as well as the periodicity (pitch a) of the SCIL-pattern have to be taken into account to explain the scattering image we obtain in figure (4.1, right picture). With a periodicity of $a = 534$nm between pillars in the hexagonal structure, the minimal reciprocal vector G_m in vacuum is

$$G_m = \frac{2\pi}{534\text{nm}}$$

G_m indicates the width of the first Brillouin zone (M-symmetry point). The PL emission spectrum of which an energy range ΔE results from is shown in figure 4.2. As one can

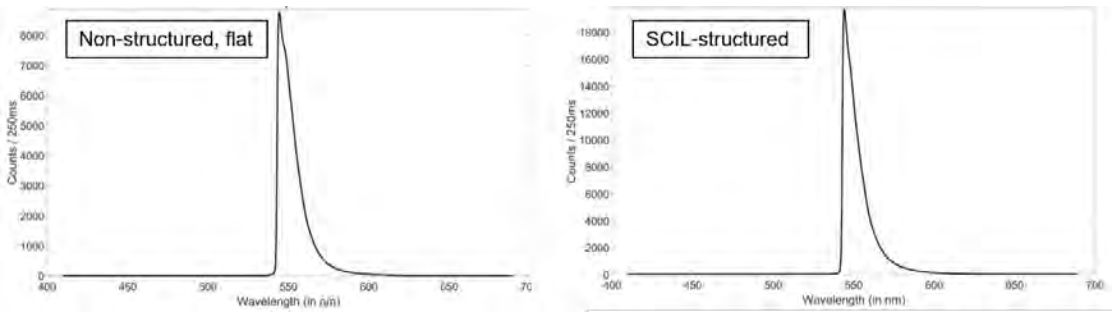

Figure 4.2: PL spectrum ΔE of SCIL-structured perovskite layer (right) and flat perovskite layer (left) on glass. The usage of the 534nm long-pass filter cuts off the majority of the PL emission, as the maximum of the PL spectrum is located at ≈ 534nm.

observe in figure 4.2, the PL spectrum is at a range of $\Delta\lambda = 540\text{nm} - 600\text{nm}$.

The range of wavelengths $\Delta\lambda$ in the PL spectrum at which intensity $I \neq 0$ leads to a range of maximum k-parallel values in the experiment. Using $n = 2.2$ as the refractive index of the perovskite material, the maximum k-parallel vectors inside the perovskite structure are given by

$$k_{\text{par,max}} = \frac{2\pi}{\lambda} \cdot n$$

In the following table, the maximum k-parallel values as well as important length scales of the hexagonal reciprocal lattice are given:

Symmetry points	**Magnitude k-vector**
M	$1.29 \cdot 10^7 1/\text{m}$
K	$1.73 \cdot 10^7 1/\text{m}$
Wavelength λ in nm	**Magnitude k-vector (free dispersion)**
540 (peak in spectrum)	$2.56 \cdot 10^7 1/\text{m}$
600 (lowest energy in spectrum)	$2.30 \cdot 10^7 1/\text{m}$

Table 4.1: K-vectors corresponding to M and K symmetry points of the first Brillouin zone using a pitch of $a = 534$nm as shown in figure 2.7. Further, the maximum in-plane k-vectors are calculated for the intensity maximum of the PL spectrum (540nm) and the lowest energy (600nm) in the spectrum using the free photon dispersion relation.

As dispersion of photons inside the lattice differs from free photon dispersion, the k-parallel values given in table 4.1 serve as an upper limit of possible in-plane k-vectors. With regard to the upper limit approximation of the maximum k-parallel vector which corresponds to $\lambda = 540$nm, we can expect that modes reaching far beyond the first Brillouin zone (K-point) can be observed in the in-plane k-space intensity distribution. As can be seen in figure 4.1, this can directly be verified in experiment.
To meet the Bragg-condition, the dispersion relation that determines $k_{\text{par, max}}$ has to overlap with the Brillouin-zone edges. Figure 4.3 illustrates the dispersion cross-cut (circle) of the energy which corresponds to the highest intensity in figure 4.1, located at 540nm. Figure 4.3 then matches the Brillouin zone scheme (figure 2.12) to the in-plane k-space distribution (figure 4.1) by direct comparison. From figure 4.3, one can observe a clear maximum in intensity. This is indicated by the dispersion relation cross-cut (circle)

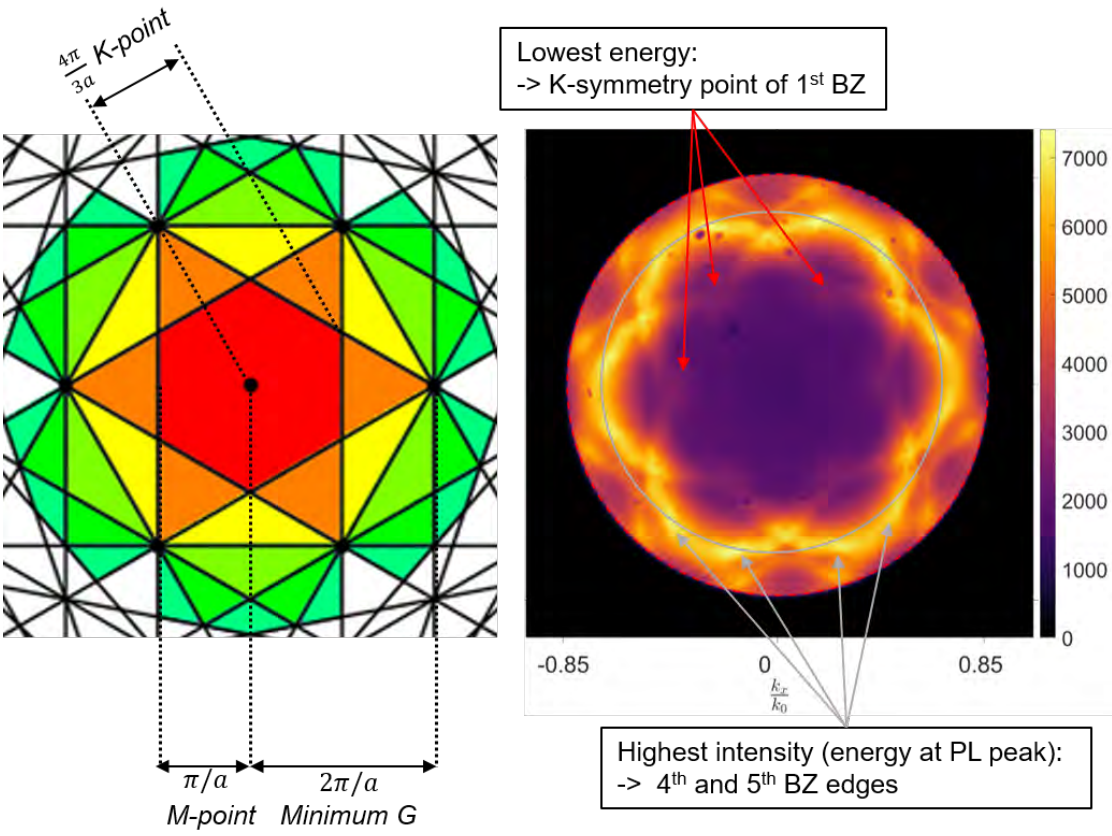

Figure 4.3: Matching of in-plane k-space distribution of scattered wave-guide modes (figure 4.1) to the Brillouin zone scheme (figure 2.12): Dispersion relation cross-cut (circle) indicates energy corresponding to highest intensity (peak in photo-luminescence spectrum).

matched to the points of highest intensity. The Brillouin zone edges appear very bright in the places where the indicated circle (figure 4.3) matches the edges at 12 distinct points. For every circle which corresponds to an energy E, a integer multiple of $m \cdot 6$ dots are visible in k-space distribution due to the reciprocal lattice of the hexagonal pattern.

Looking at figure 4.3, the hexagonal first Brillouin zone is barely visible. However, the K-symmetry points can be observed yet very low in intensity. These points are ordered hexagonally as predicted by the shape of the first Brillouin zone. The wavelength which matches the K-symmetry condition is $\lambda_{\mathrm{K}} = 801\mathrm{nm}$ when calculating using the free photon dispersion relation. It is thus clear that this wavelength attribution is well off since the highest wavelength in the spectrum is around $\lambda = 600\mathrm{nm}$. Consequently, band-

bending at Bragg-planes (stop gap) has a strong influence on dispersion.
The PL spectrum shown in figure 4.6 gives an energy distribution ΔE over a range of wavelengths. As a consequence, many Brillouin zone edges should be visible in the in-plane k-space distribution as these energies all relate to different k_{par} vectors. Comparing with figure 4.3, many Brillouin zones edges are visible which can be attributed to the energy distribution ΔE. Higher order Brillouin zones are clearly visible up to the edge of the 6th Brillouin zone. Yet, high energies E do not necessarily relate to the highest in-plane k-vectors observed in the intensity distribution and vice versa. This is due to the non-linear band-structure which features several energy branches (figure 4.4). The highest intensity in the in-plane k-space plot is indicated in figure 4.3 by the dispersion relation cross-cut (circle). The circle intersects the Brillouin zone scheme at a position which is, by bare comparison with the "perfect" Brillouin zone construction in figure 4.3, the Brillouin zone edge of the 4th and the 5th Brillouin zone. This corresponds to $k_{||} \approx 0.7 - 0.75$. One could suggest that this maximum in intensity located at the intersection of the 4th and the 5th Brillouin zone might be linked to the peak in intensity of the PL spectrum (figure 4.2) which is located at $\lambda = 540$nm. $\lambda = 540$nm would correspond to an energy of $E = 2.3$eV. We can verify that this exact energy is linked to the highest intensity observed and indicated in figure 4.3 (circle) by looking at the dispersion plot of the patterned side of the sample in figure 4.2. As we can clearly see for

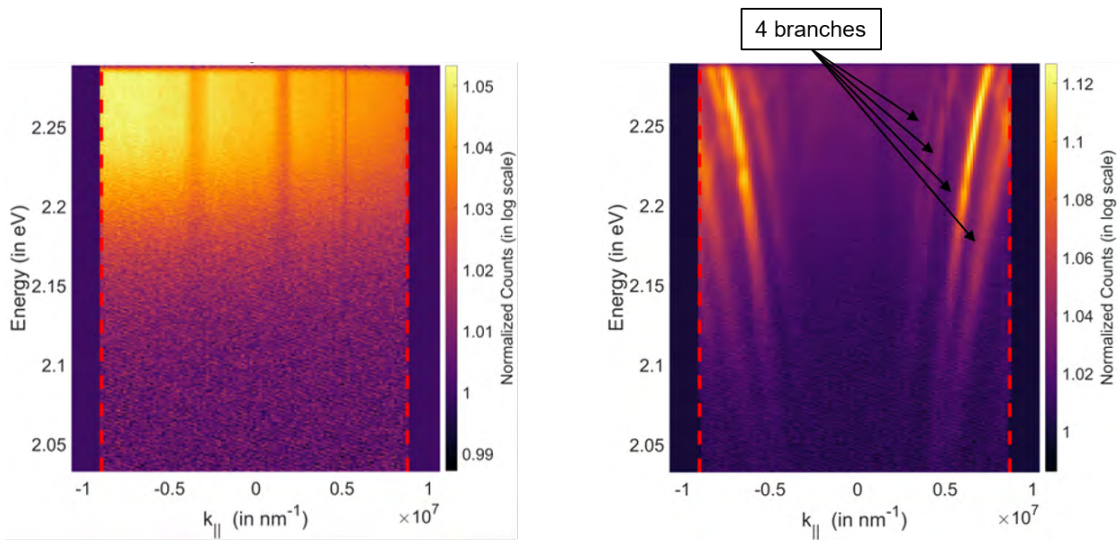

Figure 4.4: Dispersion of the observed in-plane k-space distribution shown in figure 4.1. Left side: Dispersion of non-structured sample plotted over k-parallel fraction. Right side: Dispersion of SCIL-patterned sample plotted over k-parallel fraction. The highest intensity seen at $E = 2.25$eV corresponds to $\lambda = 550$nm.

the dispersion of the SCIL-structured sample (right picture), the highest intensity refers to an energy of $\approx 2.2\text{eV} - 2.3\text{eV}$ or a wavelength of $\approx 550\text{nm} - 540\text{nm}$ at $k_{\|} \approx 0.75$. When comparing with the PL spectrum in figure 4.2 where the peak intensity is located at $\lambda = 540\text{nm}$, is shows that the intensity distribution of the PL spectrum is closely related to the intensity spectrum in the in-plane k-space distribution.
Still, we can also observe k-parallel vectors even surpassing the intensity maximum indicated in figure 4.3 (circle). But as we have just shown, the intensity maximum relates to the shortest wavelengths of the spectrum ($550\text{nm} - 540\text{nm}$). Argumentation using linear photon dispersion leads to a contradiction here. As photon dispersion inside the SCIL-pattern does not follow $E \propto k_{\text{par}}$ as can be clearly seen in the dispersion plot (figure 4.4), the non-linear and more dense photon band-structure (4 branches visible for positive $k_{\|}$) inside periodic lattices explains why k-parallel vectors higher than the intensity maximum are visible. We can conclude from the dispersion plot of the in-plane k-space distribution (figure 4.2) that dispersion organizes in branches. Further, the tendency that higher k-parallel values relate to higher energies is true for each individual branch, yet it is wrong when looking at the whole dispersion relation. Thus, the edge of the k-space plot ($k = 0.85k_0$) does not relate to the highest energy in this case as an example. This more complex band-structure explains why we see Brillouin zone edges beyond the k-parallel value which shows highest intensity (indicated by circle in figure 4.3). Interestingly for low $k_{\|}$ magnitudes, no energy branch is visible in figure 4.4. This is a consequence of the Bragg-condition which starts at the M-point of the 1st Brillouin zone.
As a conclusion, our qualitative approach of explaining k-space resolved PL images with the use of free photon dispersion to estimate the k-parallel values, the predictions for the resulting k-space distributions based on Brillouin zone edges are strikingly accurate. Starting at the K-symmetry point of the first Brillouin zone, a sharp depiction of the 2nd Brillouin zone up to parts of the edges of the 5th to the 6th Brillouin zones are visible due to the PL spectrum which provides an energy distribution ΔE. This prediction was only based on the intersection of the free photon dispersion with the extended Brillouin zone scheme, as the Bragg condition brings up dense local fields at the edges of the Brillouin zones. Thus it is shown that starting with the free photon dispersion and the extended Brillouin zone scheme, this relatively simple model introduced by [GBL$^+$21] serves for accurate prediction of possible k-space distributions of scattered wave-guide modes.
Now that we have measured the dispersion as shown in figure 4.4, we can even match parts of the branches in the dispersion relation to the Brillouin zone edges. For example, the innermost branch which is related to the smallest k-parallel vectors is responsible

for the K-symmetry point of the 1st Brillouin zone. Yet as already discussed, the Bragg-condition at the K-point of the 1st Brillouin zone does not correspond to the lowest energy value as shown in the dispersion plot (figure 4.4).

Adding a PVK hole transport layer underneath the $MAPbBr_3$ layer, the in-plane k-space intensity distribution changes slightly as shown in figure 4.5. Introducing a PVK

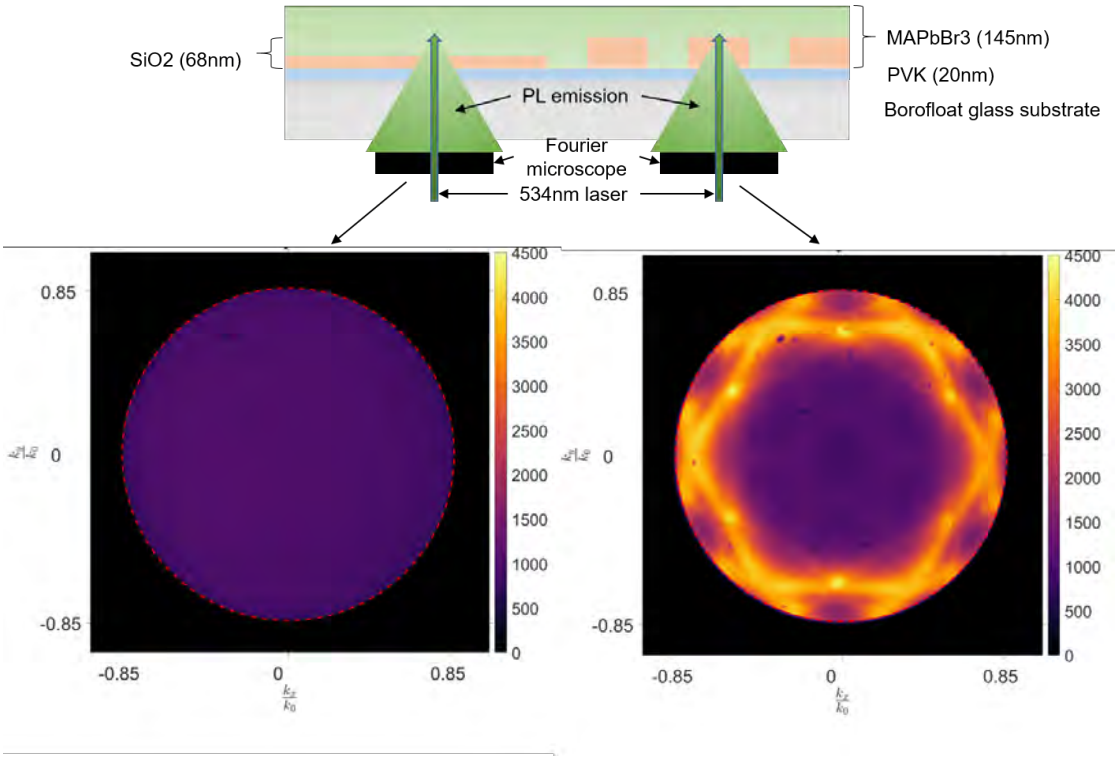

Figure 4.5: In-plane k-space resolution $(\frac{k_x}{k_0}, \frac{k_y}{k_0})$ of SCIL-patterned (right side) and non-patterned (left side) $MAPbBr_3$ on borofloat glass with one-sided PVK transport layer. Numerical aperture of objective is NA = 0.85. Distinct scattering pattern visible for the SCIL-structured active layer, non-structured layer with more homogeneous scattering.

layer, a semi-conducting material is added. Before, we only discussed the active layer ($MAPbBr_3$) in combination with the insulating SCIL-pattern (SiO_2) and the insulating glass substrate. In this situation now, a hetero-junction is created on the perovskite-PVK interface and the electric structure changes to an open-circuit voltage $\neq 0$. As PVK features a refractive index of $n = 1.56$ compared to $n = 1.42$ measured for the SCIL-pattern, the wave-guiding $MAPbBr_3$ material is now surrounded by a higher index material which should also change wave-guide modes. To verify this assumption,

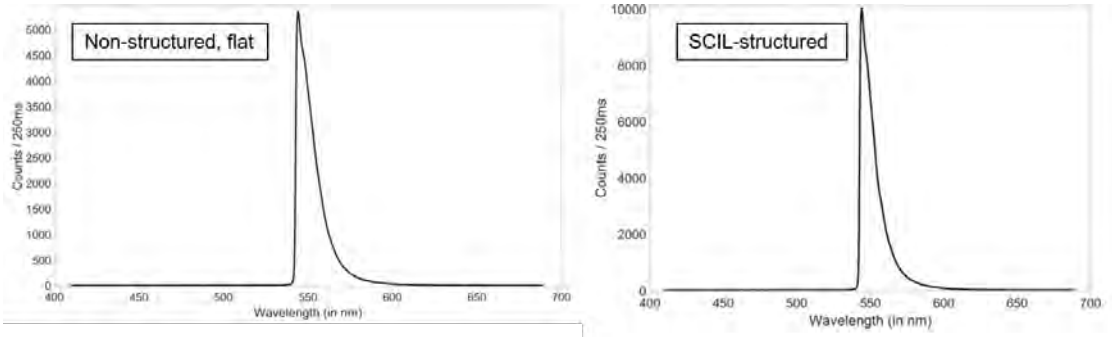

Figure 4.6: PL spectrum ΔE of SCIL-structured perovskite stack (right) and flat perovskite stack (left) as shown in figure 4.5. The usage of the 534nm long-pass filter cuts off the majority of the PL emission, as the maximum of the PL spectrum is located at $\approx$ 534nm. The spectrum is lower in intensity when compared to figure 4.2. Yet, the width and slope of the spectrum remain the same.

theoretical modeling of the wave-guide would be needed.

In a first comparison of the stack featuring PVK (figure 4.5) to the stack only featuring perovskite on glass (figure 4.1), it shows that the absolute number of counts in the intensity plots drops significantly for the PVK sample. We attribute this to PL quenching, either by charge migration to the PVK layer or by an inhomogeneous, error-prone PVK-perovskite intersection. As can be seen in figure 4.5, only the SCIL-patterned side of the sample makes direct contact with the underlying PVK layer. However, both k-space distributions shown in figure 4.5 show PL reduction by a factor of ≈ 0.7. This could be attributed to the high diffusion length of the charge-carriers. Further, as the remaining SiO_2 layer on the non-structured side is very thin, it might also feature carrier paths through the insulating SiO_2.

Light-outcoupling improvements due to the SCIL-pattern remain at a factor of ≈ 2 for the PVK-containing samples. This can be seen by comparing the PL-spectra of the SCIL-structured sample and the non-structured sample as shown in figure 4.6.

The escape cone is not significantly changed due to the PVK layer. This can be explained by the following: The PVK layer is sandwiched by silicon dioxid pillars of the SCIL pattern ($n_{SiO_2} = 1.42$) and the glass substrate ($n_{glass} = 1.47$). As their refractive indices are approximately the same, the escape cone remains. Thus, the escape cone is not an argument to explain the decrease in PL intensity when comparing the sample containing PVK (figure 4.5) to the PVK-free sample (figure 4.1).

Looking at the scattering image of the SCIL-patterned side (figure 4.5, right picture), we obtain a rather similar scattering distribution of wave-guide modes when comparing

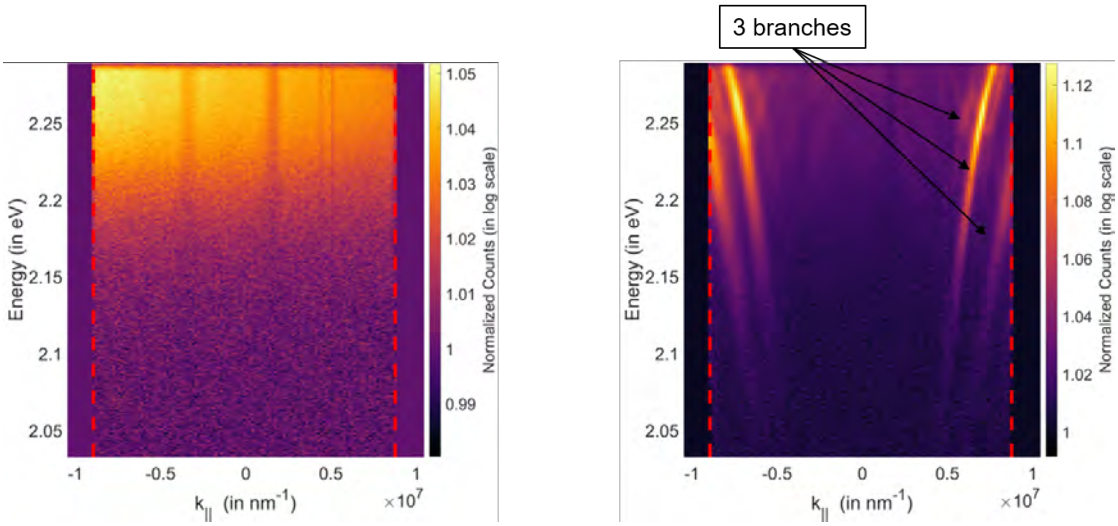

Figure 4.7: Dispersion of the observed in-plane k-space distribution shown in figure 4.5. Left side: Dispersion of non-structured sample plotted over the k-parallel fraction. Right side: Dispersion of SCIL-patterned sample plotted over the k-parallel fraction.

to figure 4.1. As the pitch a of the perturbation pattern is not changed between samples, we expect the Brillouin zone edges to appear at the same k-parallel values.

A similarity between the patterned PVK-containing sample (figure 4.5, right picture) and the patterned PVK-free sample (figure 4.1, right picture) can be seen at the intersection of the 4th to the 5th Brillouin zone. At this Brillouin zone intersection, both are very bright in intensity. This suggests that the PL spectrum is not significantly changed when adding a PVK layer. When comparing the spectra of this sample (containing the PVK layer, figure 4.6) to the spectra shown in figure 4.2, only differences in intensity through quenching can be observed. The PL distribution remains the same.

Yet, there are also clear differences comparing the in-plane k-vector distribution of figure 4.5 (PVK sample) and figure 4.1 (perovskite on glass). Most notably, this concerns the 1st and 2nd Brillouin zone edges. The 1st and 2nd Brillouin-zone edges are only visible for the sample which features patterned perovskite on glass. Adding a PVK layer, the 1st and 2nd Brillouin zone edges vanish. This can be explained by the dispersion plot of the PVK-containing sample in figure 4.7, since the energy branches for small k-parallel vectors are not present with a PVK layer. Energy branches of low k-parallel vectors only appear in the PVK-free stack. As the perovskite material and the thickness of the wave-guide remain the same, the PVK layer might change the wave-guide mode profiles inside the perovskite layer. This behavior was observed in work by [Sch16]. Quantitative modeling of wave-guide modes for the PVK-free and the PVK-containing samples

would be needed to compare or explain these differences in dispersion between the stack containing a PVK layer and the PVK-free stack in more detail.

As a last step, scattering of wave-guide modes is investigated by adding an electron injection layer (TPBi) and an aluminum back-side electrode. Thus, distinct wave-guide mode scattering is also shown on a complete stack. The results on the complete stack are shown in figure 4.8.

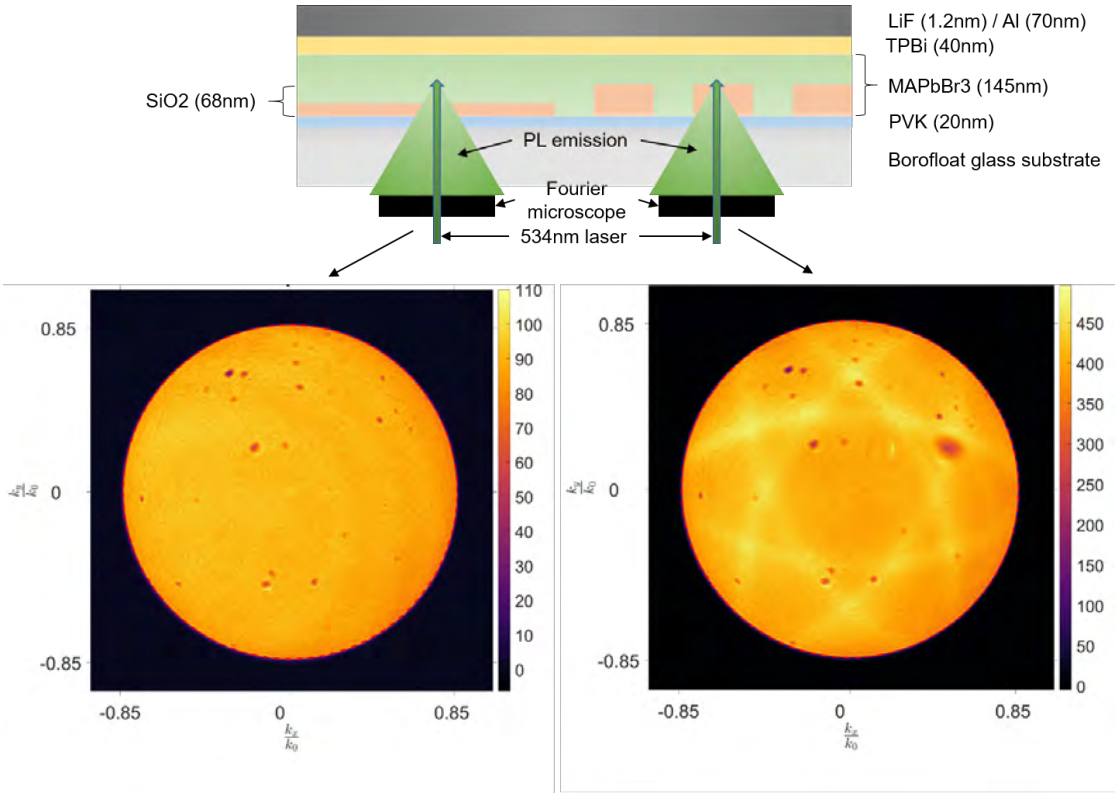

Figure 4.8: In-plane k-space resolution ($\frac{k_x}{k_0}, \frac{k_y}{k_0}$) of SCIL-patterned (right side) and non-patterned (left side) full stack as shown in figure 3.2. Numerical aperture of objective is NA = 0.85. Distinct scattering pattern visible for the SCIL-structured active layer, non-structured layer with more homogeneous scattering.

Comparing the in-plane k-space photo-luminescence intensity in figure 4.8 to the two stacks (figures 4.1, 4.5) which have been already discussed, intensity is heavily diminished when measuring on the full stack. At first, adding the TPBi layer ($n = 1.75$) to the backside of the perovskite layer transfers a significantly higher fraction of light to the back-side electrode. Secondly, the system of a perovskite layer sandwiched by a hole injection layer and an electron injection layer features an open-circuit voltage

which might induce carrier drifts during pulsed excitation (kHz laser) which could have degraded the system. Further, the layer intersections might be error-prone and thus open new recombination paths.
The interpretation of the in-plane k-space distribution is more complicated. We expect the same escape cone as in the previous experiments as only the TPBi and the Al layers are added. Further, we expect the same position of the Brillouin zones as the pitch a remains the same. Looking at the upper scattering image of the patterned full stack, the 1st and 2nd Brillouin zones are entirely visible. We can thus conclude that for the wave-guide system of PVK- $MAPbBr_3$ - TPBi, the photon dispersion inside the SCIL-pattern shifts to lower in-plane k-vectors compared to the other stacks measured. For $k_{\parallel} > 0.8$, the distinct scattering pattern vanishes as shown in the upper figure, possibly being cut off by the filter as a consequence of the dispersion relation in this stack. Unluckily, this cannot be directly proven in a dispersion plot as we did not measure it. Yet it is likely that the photon dispersion looks different in this case because the wave-guide system is changed. The previously discussed wave-guides consisted of the $MAPbBr_3$ layer ($n = 2.2$) which was sandwiched by air ($n = 1$) on the one side and glass ($n = 1.47$) or PVK ($n = 1.56$). When looking at the full stack however, the $MAPbBr_3$ layer is enclosed by PVK ($n = 1.56$) and TPBi ($n = 1.75$).

To conclude the analysis on in-plane k-space distributions of photo-luminescence, it was shown that distinct wave-guide mode scattering could be observed and qualitatively predicted using the model of free photon dispersion together with Bragg-conditions on Brillouin zone edges. Further, the highest intensity in the PL spectrum could be attributed to the highest intensity observed in the k-space distribution. Yet the highly complex band-structure which was measured makes interpretation and design of patterns more difficult as the photon energy E does not proportionally correlate to the in-plane k-vectors. Further, detailed modeling of wave-guide modes for each stack would enhance depth in analysis.
Despite all that, the proof of concept on the usability of wave-guide mode scattering in further application is given by this analysis. The loss mechanism of wave-guiding is thus turned into a useful property of the sample as the emission angles can be controlled by pattern engineering. Depending on the emission spectrum, the periodicity of the pattern as well as the dimensions of the wave-guide and the properties of the surrounding materials have to be chosen correctly. Increasing the pitch a will shift the in-plane k-space distribution towards higher Brillouin zones and vice versa. Depending on the dimensions of the wave-guide and the wavelength spectrum $\Delta\lambda$, different modes

are allowed, leading to different in-plane k-vector distributions. If for example the 30° light-cone should be enhanced by pattern design, the pitch should be risen, thus shifting the in-plane k-space distribution towards higher order Brillouin zones. This could be favorable as the Brillouin zone scheme is more dense towards higher Brillouin zone orders. Further, wave-guide modes should be allowed which feature the lowest possible in-plane k-vectors. Thus, Bragg-conditions at small in-plane k-vectors can be met, intersecting high-order Brillouin zones. In addition, scattering is also dependent on the material used for the periodic perturbation. This has to be taken into account for the pattern design as well. As the width of the pillars does not change the pitch, the Brillouin zone edges should approximately remain at the same k-vector positions. Still, as higher width should relate to more scattering, it would be interesting to investigate if there is a balance between maximum scattering through wide pillars and enough active perovskite material between the pillars which provides for highest out-coupling.
Light out-coupling has also been quantified in this analysis. Coming up with a factor of $f \approx 2$ of intensity improvement through integrating a pattern inside the perovskite structure, it matches well with the already reported hexagonal pattern (pitch $a = 400$nm) by [SCL+19] with featured an improvement by the factor of $f = 2.1$.

Beyond the proof of concept of distinct wave-guide mode scattering and the enhanced light-outcoupling of SCIL-patterning which were shown, we now focus on the change of opto-electronic properties of SCIL-patterned perovskite layers compared to their flat counterparts. Mainly, absorption and X-ray diffraction as well as their implications for the band-gap and uniformity of the crystal lattice will be discussed. Further, carrier lifetime will be analyzed with regard to possible passivation effects of the SiO_2 pattern.

4.2 TCSPC lifetime measurements: Passivation effect through SiO_2 pattern?

The SCIL-patterned perovskite layers are also analyzed regarding carrier lifetimes. There are a few considerations going into this measurement. The model discussed in the theory section, namely equation 2.4, is employed to model carrier density $n(t)$ here. In this model's derivation, drift and diffusion terms are neglected since we assume that the E-field vanishes inside the stack. This is only the case if the perovskite layer is the only semi-conducting material in the sample. Thus, only the basic perovskite-on-glass stack is investigated in the following in order to apply the analytically solvable carrier-density model given in equation 2.4 on the measurements. By fitting this model to the data, the TPL-decay of the SCIL-patterned side (red) and the non-structured side (black) is

plotted in a ln-scale over time t in figure 4.9. A cycle duration of $t = 120$ns is used for the TPL signal to reach noise level again after excitation. Thus, no build-up effects occur.

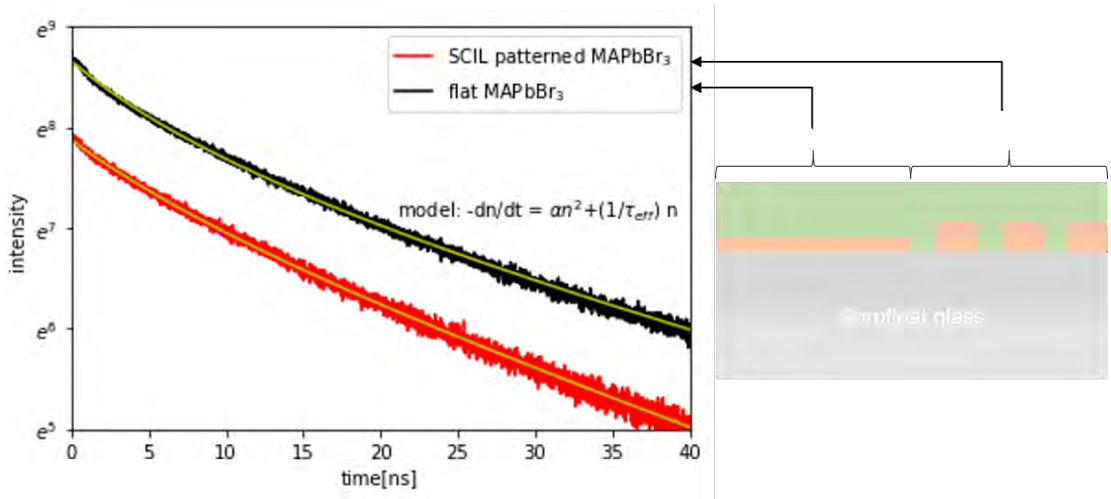

Figure 4.9: TCSPC photo-luminescence decay: SCIL-patterned $MAPbBr_3$ layer on glass (red) and flat $MAPbBr_3$ on glass with residual SiO_2 layer (black), fitted using the following ODE: $-\frac{\mathrm{d}n}{\mathrm{d}t} = \alpha n^2 + \frac{1}{\tau_{eff}} n$. Fit is indicated in yellow. The fit was conducted over a range of 50ns as for $t > 50$ns, the decay peak relaxed to a high noise level.

Parameters of TCSPC fit	SCIL-structured $MAPbBr_3$	flat $MAPbBr_3$
Radiative: $\alpha = k_{\mathrm{rad}}(1 - q_{\mathrm{int}})$	$2.270(16)^{-5}$	$1.6130(68)^{-5}$
SRH lifetime: $\tau_{\mathrm{eff}} = \tau_{\mathrm{n}} + \tau_{\mathrm{p}}$	18,38(25)ns	24,57(30)ns

Table 4.2: TCSPC modeling from figure 4.9: parameters for the radiative coefficient α and the combined SRH-lifetime τ_{eff}

The PL intensity in TPL measurements is proportional to n^2 as radiative recombination is a bimolecular process. Thus in a logarithmic plot of the intensity decay, linear slopes indicate that SRH-recombination dominates as SRH recombination relates to a mono-exponential decay (compare to model shown in figure 4.9). Non-linear slopes indicate the domination of higher-order recombination mechanisms, mainly radiative recombination. As can be seen in figure 4.9 and the parameters given in table 4.2, the fit shows proper conformity to the data. Thus we can conclude that the model which only takes two recombination paths into account resembles the recombination process well. Comparing the TPL decays, interesting differences occur between the SCIL-patterned and the

flat sample. At first, PL intensity of the non-patterned sample (black) is higher by the magnitude of $\approx e$ compared to the patterned sample (red) for the same excitation pulse. Further, as the calculated SRH-lifetime of the SCIL-patterned sample (red) is lower, trap-assisted recombination leads to a steeper linear domain at $t > \tau_{eff}$. Thus, the progression of intensity over time drifts further apart for higher t values. This might show that the SCIL-pattern leads to more induced trap-states inside the perovskite layer. One still has to investigate if these trap-states would either result from the passivation properties of the SiO_2 pattern or rather from growing a $MAPbBr_3$ layer on top of a structure: More induced trap-states could be explained by bad passivation properties of the SiO_2 of which the SCIL-pattern consists, possibly rough surface morphology. Further, it could also be explained by trap-states which might form when the perovskite layer crystallizes inside the patterned SiO_2 as crystallization might not be as homogeneous inside the pattern.

Radiative coefficients α do also differ. According to theory, this might lead to the following: As the radiative coefficient is higher for the SCIL-structured sample (red), the domain of a non-linear decay owing to radiative recombination is shifted to smaller time-scales as shown in figure 2.6 in the theory section. Thus, a non-linear decay can barely be observed for the red curve. The decay is quasi-linear for $t > 10ns$ (red). For the non-structured sample (black) instead, a lower radiative coefficient α combined with a higher SRH-lifetime leads to a large non-linear domain in figure 4.2. This is further enhanced by a higher initial carrier-concentration as the initial PL intensity is higher for the non-structured sample. The fact that higher initial carrier-concentration leads to non-linear slopes in the ns time-domain can be seen in figure 2.5 of the theory section. We might conclude that radiative recombination dominates over larger time-scales in the non-structured sample whereas in the patterned sample, SRH-recombination dominates at earlier stages. Concerning the non-structured sample, it is yet hard to distinguish if rather the effect of higher initial charge-carrier density or the effect of a lower radiative coefficient α and a higher SRH-lifetime τ_{eff} caused this non-linear slope (black).

The carrier-lifetime analysis is crucial for the feasibility of the silica-based solgel imprint that were used in these experiments. As SRH lifetime is lower for the SCIL-patterned samples, further investigation is needed if this results from the passivation properties of the SiO_2 pattern (material propert SiO_2) or if this rather results from the fact that a perovskite layer was grown on top of a structure which might have induced inhomogeneities (material property structured perovskite layer). All this data was measured on the same excitation density. It would be necessary to perform TCSPC measurements on different excitation densities in order to better distinguish between the radiative coeffi-

cient α and the SRH lifetime and also to investigate how α and τ_{eff} evolve for different fluences. As SRH lifetimes are reported to be situated in the high ns-range for large crystals, the SRH-lifetime values obtained by ODE-fitting in this analysis go well with the low grain-size of the perovskite crystals inside the $MAPbBr_3$ layer (figure 3.7).

4.3 UV-vis analysis: Absorption edge and band-gap

UV-vis steady state absorption measurements were performed for wavelengths of $\lambda = 250\text{nm} - 800\text{nm}$. At first, a Tauc plot is fitted to the absorption edge in order to calculate an approximate of the band-gap energy E_G. This is shown in figure 4.10.

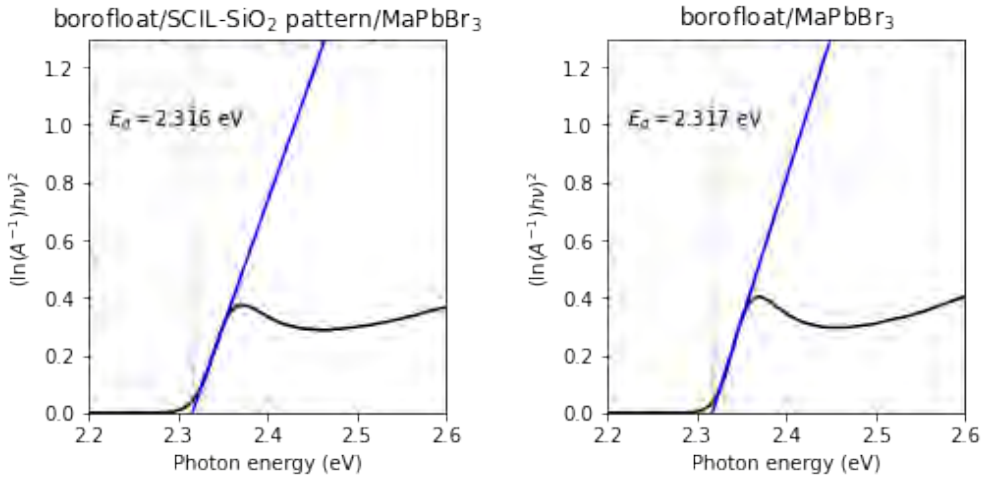

Figure 4.10: UV-vis absorption edge fit using a Tauc plot: SCIL patterned sample (left) and non-patterned sample (right)

As expected, the SCIL-pattern does not change the location of the absorption edge. Thus, a similar band-gap energy $E_G = 2.32\text{eV}$ is found in both cases. This band-gap energy is well comparable with band-gap energies of $MAPbBr_3$ in literature [LAA+16]. Also when changing band alignment through adding a PVK layer between the borofloat glass and the SCIL-patterned perovskite layer, the band-gap energy remained at 2.32eV. Thus, there is no effect related to the SCIL-pattern which changes the band-gap energy. This suggests that the nature of crystallization between flat and patterned perovskite layers does not change which is important for the applicibility of the SCIL-patterning technique in perovskite layers.
However, a change in absorption between SCIL-patterned and non-patterned samples is measured at photon energies higher than $E_G = 2.32\text{eV}$. This is presented in figure 4.11.

Figure 4.11 shows distinct absorption differences for energies $E > 3.2$eV ($\lambda = 388$nm).

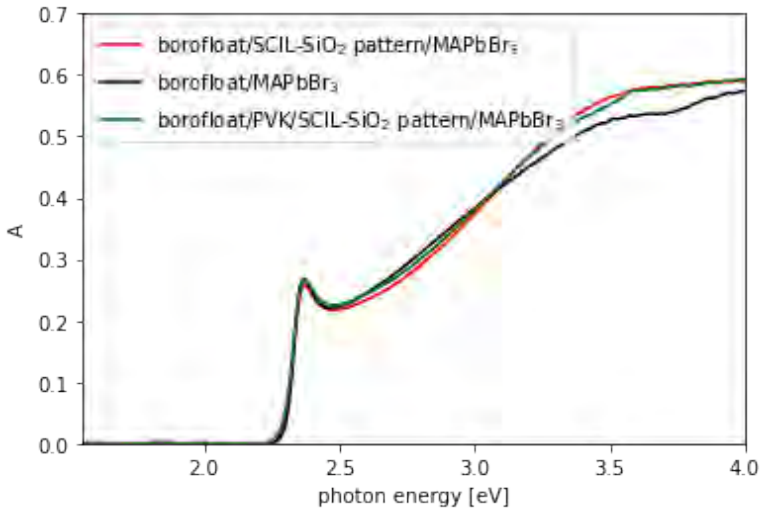

Figure 4.11: UV-vis absorption differences using no pattern, a SCIL-pattern and a SCIL-pattern with underlying PVK

As both SCIL-patterned samples (red line and green line) show higher absorption for $E_G > 3.2$eV, it is not an effect which can be attributed to the underlying PVK layer (green line) and thus changed band alignment at the PVK-$MAPbBr_3$ interface. It is rather a direct effect of the SiO_2 pattern itself. As a conclusion, the UV-vis experiments show no change in band-gap energy E_G caused by patterning, but absorbance differences which can be directly linked to the pattern. These findings motivate to think about patterns which specifically absorb perpendicular incident light. Enhanced absorbance could thus be used for solar cell application. In this particular case already, there would be a $\approx 5 - 10\%$ absorbance increase in the spectrum of $\lambda = 290 - 390$nm.

4.4 XRD analysis: Differences in crystallization?

For XRD analysis, this discussion focuses on the comparison of a half patterned stack of type (B) as depicted in figure 3.3 only. Every statement made hereafter also holds for adding a PVK layer to the stack as presented in figure 3.3 (stack A) as PVK did not change XRD results.

XRD scans for both the SCIL-patterned perovskite layer as well as the flat perovskite layer are shown in figure 4.12. Owing to the cubic conventional cell of $MAPbBr_3$, the (100) and (200) peaks can be clearly observed in XRD. As only these peaks occur, a strong preferential orientation of the crystals alongside the surface of the substrate can

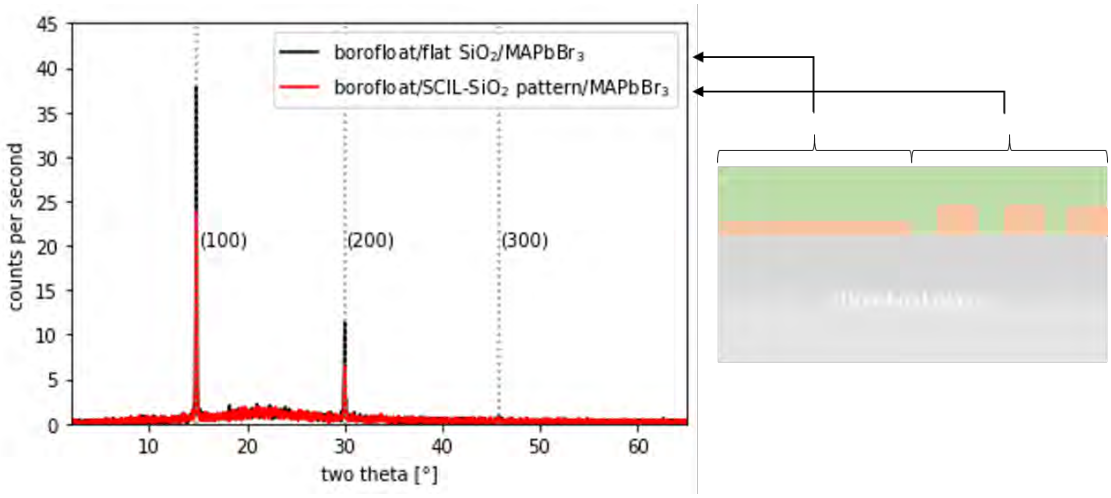

Figure 4.12: XRD spectra comparison of $MAPbBr_3$ films on borofloat glass, sample as shown in figure 3.3,(B): SCIL-structured (red line) and non-structured side (black line)

be concluded. Due to the amorphous borofloat glass underlying the perovskite layer, both the SCIL-patterned (red) as well as the flat (black) perovskite film show equal background scattering in the range of $2\Theta = 15 - 30°$. Thus, the penetration depth of the X-rays is larger than the thickness of the active $MAPbBr_3$ layer. Interestingly, figure 4.12 shows clear differences in absolute height at the (100) and (200) peak between the patterned (red) and non-patterned (black) side. Further, a very low (300) peak is only visible for the flat side. The presence of a (300) peak could normally be interpreted as a higher structural uniformity of the flat perovskite layer compared to the patterned perovskite layer, yet due to the (300) peak's very low intensity, it is not considered a factor for serious comparison. Despite the differences in peak height, the peak-ratios $q_{\text{SCIL}} = \frac{I_{(100),\ \text{SCIL}}}{I_{(200),\ \text{SCIL}}}$ and $q_{\text{flat}} = \frac{I_{(100),\ \text{flat}}}{I_{(200),\ \text{flat}}}$ are comparable. This rather suggests equal crystallization in surface-parallel orientation as explained in theory. To also verify the findings from figure 4.12 statistically, the mean and its standard deviation of the respective (100) and (200) peaks of various samples of type (B) both for flat and structured perovskite layers are plotted in figure 4.13. To validate comparability of both the peak-ratio of the flat and the SCIL-patterned perovskite layer, the probability for a random deviation of $q_{\text{flat}} - q_{\text{SCIL}} = -0.48 \pm 1.1$ is calculated to be $> 50\%$ in significance testing. Thus, both ratios q highly coincide. Consequently, differences in crystal orientation alongside the surface of the underlaying substrate are very unlikely. Still, the question remains how the absolute intensity differences of the (100)

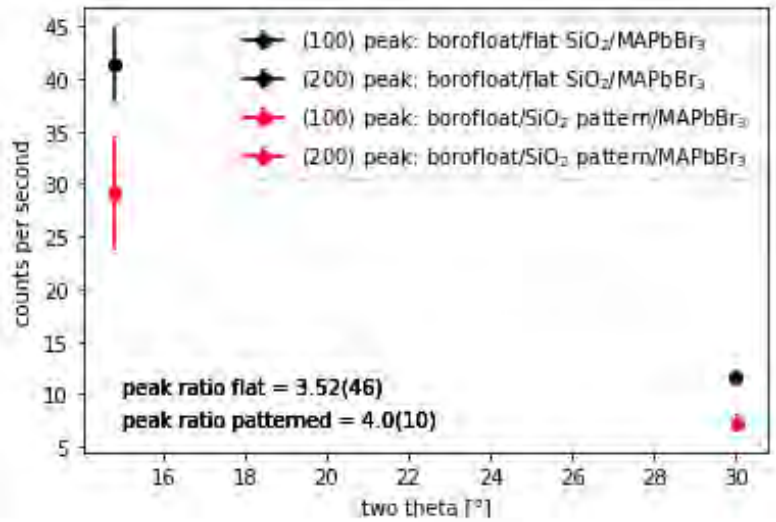

Figure 4.13: XRD peak comparison: Various samples of type (B)(figure 3.3) measured. Mean and standard deviation of (100) and (200) peaks both plotted for non-structured and SCIL-structured side of samples.

and (200) peaks of SCIL-patterned samples and non-structured samples as shown in figure 4.12 can be explained. The peak intensities for (100) and (200) differ by a factor of $a = \frac{I_{(100),\ \mathrm{flat}}}{I_{(100),\ \mathrm{SCIL}}}, a = \frac{I_{(200),\ \mathrm{flat}}}{I_{(200),\ \mathrm{SCIL}}} = 1.4 - 1.6$. Since there is no likely difference in surface-parallel crystal orientation as shown in figure 4.13 since peak-ratios q are comparable, one should look at volume differences between the SCIL and the flat $MAPbBr_3$ layers. Knowing that crystal orientation and crystallization between structured and non-structured $MAPbBr_3$ layers is comparable, we know that intensity differences are directly proportional to perovskite layer height if the penetration depth of the X-rays in XRD is larger than the perovskite layer thickness. This is the case since the background of the amorphous borofloat glass is clearly visible in figure 4.12 and equal for both the SCIL-patterned as well as non-patterned substrate. Calculating the volume difference between flat and patterned perovskite layer, we find: $v = \frac{V_{\mathrm{flat}}}{V_{\mathrm{SCIL}}} = 1.105(46)$. This would even suggest that (100) and (200) peaks of the SCIL-patterned side should be higher compared to the flat side assuming equal crystallization. As shown in figure 4.13, this is not the case. Therefore, a simple difference in volume cannot explain the observed differences in peak intensity. However, it has to be taken into account that constructive interference between planes inside the structured sample cannot take place in between the SiO_2 pillars. This is due to the difference in refractive indices between patterned SiO_2 ($n = 1.47$) and $MAPbBr_3$ ($n = 2.2$). The volume of SCIL-patterned $MAPbBr_3$

which contributes to constructive interference in XRD has to be recalculated. This is, in approximation, the volume which is not invaded by the pattern, so to speak the flat part of the SCIL-patterned $MAPbBr_3$ layer. This is shown in the following:

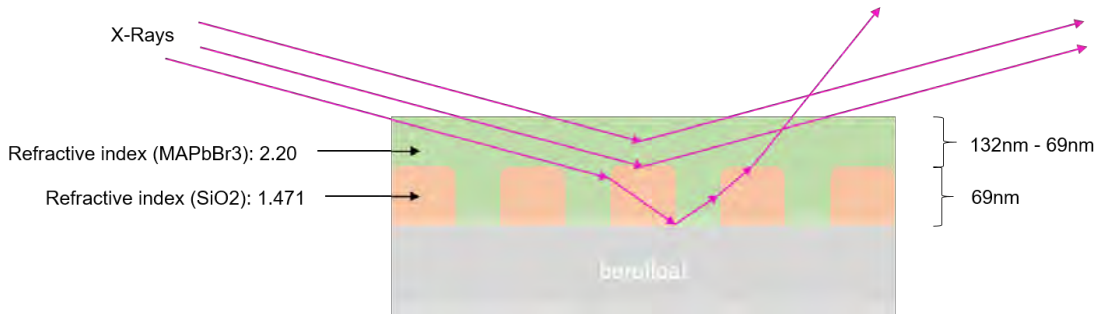

Figure 4.14: XRD in SCIL-patterned $MAPbBr_3$: constructive interference is corrupted by SiO_2 pattern. X-Rays are incident at 15° to the glass surface in this figure as an example, therefore depicting the (200) peak

Doing so, one obtains a volume ratio of $v = \frac{V_{\text{flat}}}{V_{\text{SCIL-flat}}} = 1.685(31)$. Comparing this difference in volume to the intensity-ratio $\frac{I_{(100),\ \text{flat}}}{I_{(100),\ \text{SCIL}}}, \frac{I_{(200),\ \text{flat}}}{I_{(200),\ \text{SCIL}}} = 1.4 - 1.6$, this could give a conclusive answer to the peak differences observed. However, if this is the explanation of the intensity difference between flat and patterned domains, the above findings on crystallization have to be rephrased. As no constructive XRD-signal can be gathered from between the pillars according to figure 4.14, no conclusion on crystallization of $MAPbBr_3$ between the pillars can be drawn. Comparable crystallization which was concluded only holds for the flat part of the patterned sample in comparison to the non-patterned sample.

To finalize, flat SiO_2 underlying the $MAPbBr_3$ layer did not change the XRD spectrum compared to the reference sample, featuring a bare $MAPbBr_3$ layer on borofloat glass as shown in figure 3.3(B). Thus, no additional effects in crystallization due to sol-gel can be expected.

As a conclusion, no significant differences in crystallization regarding XRD-peaks of surface-parallel planes ((100) and (200)) are observed between SCIL-structured and non-structured layers. Yet, crystallization of $MAPbBr_3$ between the SiO_2 pillars might not be measurable in XRD. Still, as the PL spectra and the band-gap energies E_G where comparable for both flat and SCIL-structured samples as shown in analysis, fundamentally different crystallization in SCIL-patterned samples is unlikely. This adds to the versatility of SCIL for application in further active perovskite layers.

5 Conclusion

In this thesis, distinct directionality of scattered wave-guide modes was proven to be a direct result of patterning the perovskite layer. Using back-focal plane imaging (Fourier microscope), in-plane k-space intensity distributions were measured and compared between SCIL-structured and non-structured samples. Up to a complete LED stack, the proof of concept on directed photo-luminescent emission was given. Thus, the loss mechanism of wave-guiding could be instead used for distinct scattering directionality out of the active layer.

From these findings, the question arises if patterns can be designed specifically for a certain goal, e.g. for higher intensity in the 30° light cone. Looking at the directionality of the scattered light, the preferred directions (k_x,k_y) at which wave-guide modes scatter were shown to be entirely predictable by the Brillouin zone edges of the lattice given by the imprinted structure. Further, it was shown that the highest intensity in the PL spectrum is related to the highest intensity observed in plane k-space. Thus, the scattering directions can be very accurately predicted if the exact $k_{\|}$-distribution inside the wave-guide is known in advance. Due to the complex photon band-structure however, it is hard to predict this $k_{\|}$-distribution in advance. As a consequence, thorough simulation on wave-guide modes as well as the photon band-structure inside the pattern-lattice has to be done in order to specifically design imprinting patterns for a distinct purpose. This could be the next step on the pathway to controlling the directionality of photo-luminescence or even electro-luminescence out of perovskite LEDs. Once the $k_{\|}$ distribution can be predicted in advance, the scattering directionality follows directly from the overlay of the $k_{\|}$ values over the Brillouin zone scheme.

We have seen that the SCIL-pattern does not severely change the opto-electronic properties of the active layer. From the band-gaps which were calculated for both patterned and flat samples and the findings on crystallization, no differences could be shown.

For lifetime measurements, more analysis under varying illumination conditions (fluences) should be done to distinguish better between the SRH-lifetime and radiative coefficients and to see how these values evolve. Yet what could be shown is that the recombination process inside the $MAPbBr_3$ layer can be described to proper accuracy by the combination of a bi-molecular and a mono-molecular process as the model based on these processes fitted the decay data well.

Overall, the fact that the band-gap and crystallization remain the same when patterning adds to the versatility of the SCIL technique when using silica-based sol-gel resists.

Wave-guide mode scattering lead to an increase in light out-coupling by the factor of 2

which has already been reported for another hexagonal pattern in literature ([MLT18]). Thus, the SCIL-imprinting technique of perovskite materials using an inorganic interlayer of SiO_2 proves as a versatile tool for light out-coupling improvement of perovskite LEDs. Thus, silica-based sol-gel resists combined with SCIL are highly promising for further application in the perovskite field.

6 Acknowledgments

This thesis would not have come about without the inspiration, the educated advice and the contribution by many friends and colleagues at AMOLF Institute Amsterdam. First and foremost, I would like to thank Loreta Muscarella for guiding me into the project and setting up the ambition of this thesis. I would like to thank Debapriya Pal who conducted all Fourier-microscope measurements based on my fabricated samples. Further, Deba's expertise in optics was one of the keys to understand and interpret the distict wave-guide scattering images presented in this thesis. I would like to thank Gianluca Grimaldi and Lucie McGovern for your advice in any perovskite-related topic and for numerous explanations and the fun and loose vibe in our office. For your educated advise and guesses and many new ideas arising from your input, I would like to thank Bruno Ehrler. I would like to thank Oscar for the most fun coffee breaks and the whole Hybrid Solar Cells group for the unforgettable time.

References

[ALM10] Aulin, Yaroslav V, M A Loi, and O V Mikhnenko: *Excitons in organic semiconductors*, 2010.

[AM20] Akkerman, Quinten A. and Liberato Manna: *What defines a halide perovskite?*, 2020. ISSN 23808195.

[ARH+19] Anaya, Miguel, Barry P. Rand, Russell J. Holmes, Dan Credgington, Henk J. Bolink, Richard H. Friend, Jianpu Wang, Neil C. Greenham, and Samuel D. Stranks: *Best practices for measuring emerging light-emitting diode technologies*, December 2019. ISSN 17494893.

[CZT+20] Cho, Changsoon, Baodan Zhao, Gregory D. Tainter, Jung Yong Lee, Richard H. Friend, Dawei Di, Felix Deschler, and Neil C. Greenham: *The role of photon recycling in perovskite light-emitting diodes.* Nature Communications, 11, December 2020, ISSN 20411723.

[GBL+21] Guan, Jun, Marc R. Bourgeois, Ran Li, Jingtian Hu, Richard D. Schaller, George C. Schatz, and Teri W. Odom: *Identification of brillouin zones by in-plane lasing from light-cone surface lattice resonances.* ACS Nano, 15:5567–5573, March 2021, ISSN 1936086X.

[GM12] Gross, Rudolf and Achim Marx: *Festkörperphysik -*. Oldenbourg Verlag, München, 2012, ISBN 978-3-486-71486-9.

[Hec18] Hecht, Eugene: *Optik -*. Walter de Gruyter GmbH Co KG, Berlin, 2018, ISBN 978-3-110-52670-7.

[JAAS21] Ji, Kangyu, Miguel Anaya, Anna Abfalterer, and Samuel D. Stranks: *Halide perovskite light-emitting diode technologies*, September 2021. ISSN 21951071.

[KCL16] Kim, Young Hoon, Himchan Cho, and Tae Woo Lee: *Metal halide perovskite light emitters.* Proceedings of the National Academy of Sciences of the United States of America, 113:11694–11702, October 2016, ISSN 10916490.

[KKL+21] Krückemeier, Lisa, Benedikt Krogmeier, Zhifa Liu, Uwe Rau, and Thomas Kirchartz: *Understanding transient photoluminescence in halide perovskite layer stacks and solar cells.* Advanced Energy Materials, 11, May 2021, ISSN 16146840.

[KMSU20] Kirchartz, Thomas, José A. Márquez, Martin Stolterfoht, and Thomas Unold: *Photoluminescence-based characterization of halide perovskites for photovoltaics*, July 2020. ISSN 16146840.

[KZXR16] Kerner, Ross A., Lianfeng Zhao, Zhengguo Xiao, and Barry P. Rand: *Ultrasmooth metal halide perovskite thin films: Via sol-gel processing.* Journal of Materials Chemistry A, 4:8308–8315, 2016, ISSN 20507496.

[LAA+16] Leguy, Aurélien M.A., Pooya Azarhoosh, M. Isabel Alonso, Mariano Campoy-Quiles, Oliver J. Weber, Jizhong Yao, Daniel Bryant, Mark T. Weller, Jenny Nelson, Aron Walsh, Mark Van Schilfgaarde, and Piers R.F. Barnes: *Experimental and theoretical optical properties of methylammonium lead halide perovskites.* Nanoscale, 8:6317–6327, March 2016, ISSN 20403372.

[LXB+21] Liu, Xiao Ke, Weidong Xu, Sai Bai, Yizheng Jin, Jianpu Wang, Richard H. Friend, and Feng Gao: *Metal halide perovskites for light-emitting diodes*, January 2021. ISSN 14764660.

[MLT18] Meng, Shuai Shuai, Yan Qing Li, and Jian Xin Tang: *Theoretical perspective to light outcoupling and management in perovskite light-emitting diodes.* Organic Electronics, 61:351–358, October 2018, ISSN 15661199.

[MPM18] Makuła, Patrycja, Michał Pacia, and Wojciech Macyk: *How to correctly determine the band gap energy of modified semiconductor photocatalysts based on uv-vis spectra*, December 2018. ISSN 19487185.

[NRE] NREL: *Best research-cell efficiency chart.* `https://www.nrel.gov/pv/cell-efficiency.html`.

[PI] PerkinElmer and Inc: *Measuring absorptance (k) and refractive index (n) of thin films.*

[Rig21] Righter, Susan: *Uvvis theory*, 2021.

[Ro0] Rohrich, Ruslan. 2020.

[SAM+15] Saidaminov, Makhsud I., Ahmed L. Abdelhady, Banavoth Murali, Erkki Alarousu, Victor M. Burlakov, Wei Peng, Ibrahim Dursun, Lingfei Wang, Yao He, Giacomo MacUlan, Alain Goriely, Tom Wu, Omar F. Mohammed, and Osman M. Bakr: *High-quality bulk hybrid perovskite single crystals within minutes by inverse temperature crystallization.* Nature Communications, 6, July 2015, ISSN 20411723.

[Sch06] Schubert, E. Fred: *Light-Emitting Diodes -*. Cambridge University Press, Cambridge, 2006, ISBN 978-1-139-45522-0.

[Sch16] Schokker, Hinke (Aaltje Hinke): *Periodic and aperiodic plasmon lattice lasers*. [s.n.], 2016, ISBN 9789492323019.

[SCL+19] Shen, Yang, Li Peng Cheng, Yan Qing Li, Wei Li, Jing De Chen, Shuit Tong Lee, and Jian Xin Tang: *High-efficiency perovskite light-emitting diodes with synergetic outcoupling enhancement*. Advanced Materials, 31, June 2019, ISSN 15214095.

[TZL+20] Tan, Dawei, Xuejing Zhang, Xiao Liu, Hongmei Zhang, and Dongge Ma: *Stability enhancement of inverted perovskite solar cells using lif in electron transport layer*. Organic Electronics, 80, May 2020, ISSN 15661199.

[VMN+17] Verschuuren, Marc A., Mischa Megens, Yongfeng Ni, Hans Van Sprang, and Albert Polman: *Large area nanoimprint by substrate conformal imprint lithography (scil)*, June 2017. ISSN 21928584.

[WCD+22] Wu, Jiaying, Hyojung Cha, Tian Du, Yifan Dong, Weidong Xu, Chieh Ting Lin, and James R. Durrant: *A comparison of charge carrier dynamics in organic and perovskite solar cells*. Advanced Materials, 34, January 2022, ISSN 15214095.

[WLSS17] Wang, Kai Hung, Liang Chen Li, Muthaiah Shellaiah, and Kien Wen Sun: *Structural and photophysical properties of methylammonium lead tribromide (mapbbr3) single crystals*. Scientific Reports, 7, December 2017, ISSN 20452322.

[WX19] Wei, Zhanhua and Jun Xing: *The rise of perovskite light-emitting diodes*, June 2019. ISSN 19487185.

[ZLR+19] Zhao, Lianfeng, Kyung Min Lee, Kwangdong Roh, Saeed Uz Zaman Khan, and Barry P. Rand: *Improved outcoupling efficiency and stability of perovskite light-emitting diodes using thin emitting layers*. Advanced Materials, 31, January 2019, ISSN 15214095.

[ZWP+17] Zardetto, V., B. L. Williams, A. Perrotta, F. Di Giacomo, M. A. Verheijen, R. Andriessen, W. M.M. Kessels, and M. Creatore: *Atomic layer deposition for perovskite solar cells: Research status, opportunities and challenges*, 2017. ISSN 23984902.

[ZZ18] Zinth, Wolfgang and Ursula Zinth: *Optik - Lichtstrahlen – Wellen – Photonen.* Walter de Gruyter GmbH Co KG, Berlin, 2018, ISBN 978-3-110-49236-1.

[ZZF+20] Zhang, Qianpeng, Daquan Zhang, Yu Fu, Swapnadeep Poddar, Lei Shu, Xiaoliang Mo, and Zhiyong Fan: *Light out-coupling management in perovskite leds—what can we learn from the past?*, September 2020. ISSN 16163028.

List of Figures

List of Tables